SYNTHESIS OF 1T-TANTALUM (IV) SULFIDE AND OBSERVATION OF CHARGE DENSITY WAVE USING SCANNING TUNNELING MICROSCOPY

BY

SUNDARAVADIVEL RAJARAJAN

THESIS

Submitted in partial fulfillment of the requirements
for the degree of Master of Science in Electrical and Computer Engineering
in the Graduate College of the
University of Illinois at Urbana-Champaign, 2015

Urbana, Illinois

Advisor:

Professor Joseph W. Lyding

ABSTRACT

Over the past decade, due to the increasing interest and urgency in finding an alternate material system for post-silicon logic and opto-electronic applications, staggering progress have been made in the study of low-dimensional materials. These low-dimensional materials not only help reduce transistor footprint and improve power and performance metrics, they also exhibit very peculiar electrical properties. A particular example is the existence of a charge density wave (CDW) in 1T-Tantalum (IV) Sulfide (1T-TaS_2). A member of the transition metal dichalcogenide (TMDC) family, 1T-TaS_2 exhibit a periodic modulation of electronic charge density. Unlike bulk semiconductor or metals, lattice distortion in this low-dimensional material creates non-uniform, wave-like electron densities.

In this thesis, we have demonstrated two bulk material growth strategies for the synthesis of 1T-TaS_2. We have successfully grown poly-crystalline 1T-TaS_2 powder through a direct solid-solid reaction and single-crystals of 1T-TaS_2 through Iodine-assisted chemical vapor transport (CVT). After a few growth setup revisions, the growth processes have given consistently high yields. Next, we performed an ultra-high vacuum scanning tunneling microscopy (UHV-STM) study of the grown poly-crystalline 1T-TaS_2. The powder was deposited onto an atomically flat, H-passivated silicon substrate using dry contact transfer (DCT), an *in-situ* deposition technique developed by the Lyding group for clean, UHV-compatible transfer of nano-materials. We managed to directly observe room-temperature CDW on the deposited nano-flakes of 1T-TaS_2. The periodicity of the CDW lattice correspond very closely to the expected $\sqrt{13}$ x $\sqrt{13}$ nearly commensurate room-temperature CDW phase.

To my loving sister, Abi. You'll forever be in our hearts.

ACKNOWLEDGMENTS

I am indebted to a multitude of people, without whom, the work presented in this thesis would have been impossible. Foremost, I would like to offer my sincere gratitude to my advisor, Professor Joseph Lyding. Over the past four years, since my undergraduate days, he has given me the freedom and autonomy to engage in various research projects. The intellectual freedom and advice he provided motivated me to strive harder and think both, creatively and independently. He cultivated a strong sense of collaboration, openness and ownership around the lab, which made it a very conducive environment for research. Under his tutelage, I have learned to critically approach, research and effectively solve problems—skills that I strive to carry and use throughout my career. I also can't thank him enough for believing in my abilities and nominating me for the ECE Departmental Fellowship. It was my great privilege to have worked with him and I will always be grateful for this wonderful experience.

Within the STM group, I have had the opportunity to work with several outstanding colleagues. The level of camaraderie in the group was admirable and made my research experience truly enjoyable. I would like to thank Dr. Justin Koepke for training me on the STM. He was very patient and thorough in conveying his knowledge and expertise, and provided me with enough confidence and freedom to operate the STM independently. In that vein, I am also very grateful to Adrian Radocea, who was instrumental in the success of the STM work. He taught me the nuances of sample preparation, tip etching and tricky LTM maneuvers. I also thank Dr. Joshua Wood, a former member of the group, for being a motivational figure. I have always been in awe at his child-like curiosity and

passion for science and engineering, and hope to embody it through my future endeavors. Furthermore, I owe many thanks to Dr. Jae Won Do, my graduate student mentor during undergraduate research, who encouraged and supported me through my research. I also wish to thank Torin Kilpatrick for sharing his knowledge on DCT and TaS_3, which proved influential in my study of TaS_2. I thank all former and present members of the STM group for their support and helpful ideas. I couldn't have asked for a better research group.

I also wish to thank the ECE faculty and its members for shaping my academic career over the last six years. The faculty has inspired me towards success and has cultivated an undying passion for the field of electrical engineering. Special mention goes to Professor Elyse Rosenbuam, Professor Pavan Kumar Hanumolu and Professor Chandrasekhar Radhakrishnan. Professor Rosenbaum's classes were some of my most favorite classes at UIUC. Her classes empowered me with the necessary skills for success in both, academics and research. Along with Professor Rosenbuam, I also thank Professor Hanumolu and Professor Radhakrishnan for providing me an opportunity to be a part of their course staff. Being a teaching assistant didn't just provide financial assistance throughout my graduate studies, it also gave me a sense of pride to share my passion and love for this field of study.

I am also truly grateful for the friends I made in graduate school. Their encouragement and support motivated me to strive for the best. Being from different technical backgrounds, they provided very refreshing takes on how to approach and solve problems, which directly influenced my work greatly. Special mention goes to Aparna Lankupali Uvaraj for helping with the editing and providing constructive criticism on the graphics presented in this thesis. I also thank Sabareeshkumar Ravikumar, a fellow ECE graduate student, for patiently listening to the problems I faced during my thesis research and providing not just technical advice/suggestions, but also comical relief through his Vadivelu humor. Last but not least, I would like to sincerely thank my parents and all of my family for their love, support and belief. Their constant encouragement and unconditional love has made me the person I am today.

TABLE OF CONTENTS

CHAPTER 1

INTRODUCTION

Two-dimensional (2D) materials have been extensively investigated due to the wealth of unusual physical phenomena that occur when charge and heat transport is confined within a 2D plane. The interest in these lower-dimensional materials has been piqued further as we begin to approach the fundamental scaling limits of silicon integrated circuits (IC). In this chapter, we first survey the historical trend in complementary metal-oxide-semiconductor (CMOS) scaling and motivate the need for alternative material systems. We then review certain 2D material systems, mainly transition metal dichalcogenides (TMDCs), which could potentially continue to extend the scaling roadmap. Large-area, low-cost, high-yield growth and fundamental understanding of this class of material will prove crucial for the success of TMDCs in the post-silicon era. To this end, we will evaluate several state-of-the-art bulk and thin-film synthesis schemes, and access their merits and demerits. Finally, we will probe further into a certain type of TMDC and conclude the chapter with a review of the charge density wave phenomenon in the material of interest, tantalum (IV) sulfide or tantalum disulfide (1T-TaS_2).

1.1 Moore's Law and Si-CMOS Scaling

Since the invention of integrated circuits (IC), solid-state device scaling has helped the IC industry steadily improve cost, power and performance metrics. As a result, the semiconductor industry has aggressively driven transistor feature size from 10 µm to 14 nm during the last 40 years. As we near the end of the silicon roadmap, we are fast approaching a fundamental scaling limit with traditional

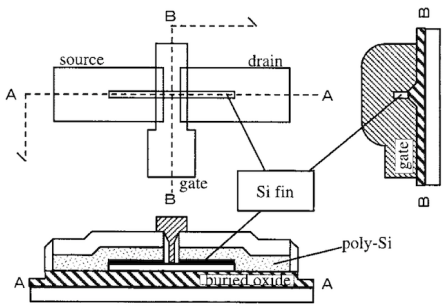

Figure 1.1: Typical layout and cross-section of FinFET device [1].

silicon complementary metal-oxide-semiconductor (CMOS) technology. The introduction of new device concepts and/or new material systems might soon become inevitable to sustain Moore's law, which states the number of transistors on a chip of a given size roughly doubles every two years.

In a bulk-Si device, detrimental short-channel effects, such as drain-induced barrier lowering (DIBL), occur when the lateral electrical field becomes comparable to the vertical electrical field. Continuous lateral and vertical field scaling with traditional planar Si-CMOS has become increasingly challenging due to various limitations. In 2008, in order to continue oxide thickness scaling, the industry migrated from SiO_2/poly-Si gate stacks to high-K dielectric/metal gate stacks. After decades of planar transistors, the IC industry opted to FinFET devices for $<$22 nm technology nodes (Fig. 1.1); this wrap-around gate device structure helped greatly reduce off-state leakage and mitigate short-channel effects. Although these novel device structures have successfully driven transistor miniaturization in the last decade, silicon is fast running out of steam. Researchers worldwide are investigating various nano-materials with desirable properties that could propel the IC industry into the sub-10 nm regime.

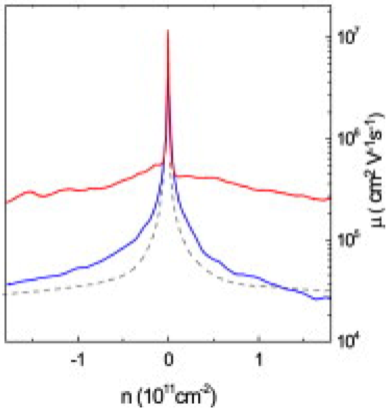

Figure 1.2: Plot of mobility, μ, as a function of carrier density n for suspended graphene [2].

1.2 The Rise of 2D Materials

In 2010, Andre Geim and Konstantin Novoselov won the Nobel Prize in Physics for their groundbreaking experiments regarding graphene. Due to its atomistic nature and exemplary carrier transport properties, graphene, a tightly bound one-atom thick layer of sp2 carbon, has garnered a growing interest in the hunt for new materials for the post-silicon era. One of the most enticing attributes of graphene is its linear energy-momentum relationship for electrons (holes) in the conduction (valence) band. Unlike silicon's quadratic energy dispersion relationship, graphene's linear energy-momentum relationship gives rise to carrier mobility that is orders of magnitude larger than that of silicon. This could have major implication for the semiconductor industry as it allows for, at least in principle, all-ballistic devices. Experimental mobility measurements from mechanically exfoliated, suspended graphene coincides closely with theoretical predictions (Fig. 1.2). Another interesting observation of graphene's charge transport is its ambipolarity; graphene's unique band structure allows for electron or hole conduction depending on the position of the Fermi level with respect to the Dirac point (Fig. 1.3). By electrostatically controlling doping, we can jettison the need for acceptor/donor impurities, which would serve as scattering sites for carriers during device operation.

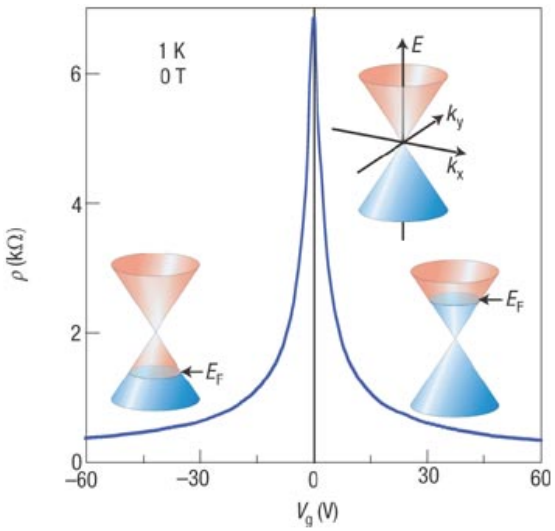

Figure 1.3: Conical low-energy spectrum E(k), indicating changes in the position of the Fermi energy E_F with changing gate voltage [3].

Although these unique qualities make graphene a promising candidate for post-silicon applications, there are several limiting factors hindering the rise of graphene. One of the major concerns is that graphene is intrinsically a zero bandgap semimetallic material. Without a bandgap, despite its excellent mobility, graphene serves as a poor substitute for silicon in logic/switching applications. Bandgap engineering by quantum size confinement, external electric field and strain have been demonstrated by various groups. Scalability of such methods is proving to be a bottleneck in the development of graphene. Large-scale, high-quality, high-yield synthesis of graphene is also another challenge that is being currently being addressed by the research community. In this respect, wide variety of reasonably successful growth techniques have been demonstrated. Chemical vapor deposition (CVD) of hydrocarbon on catalytic metals, such as Cu and Ni, is a very popular technique for large-area synthesis [4–6]. Graphitization of SiC in ultra-high vacuum at high temperature also gives rise to graphene layers on the insulating SiC substrate [7]. Apart from these large-area synthesis, bottom-up synthesis of graphene nano-structures using molecular precursors has also been successfully demonstrated by various groups [8, 9]. The outstanding progress in graphene research over the last decade has been truly staggering.

In view of the success obtained in the search of viable exfoliation, growth, transfer techniques, the ideologies and methodologies learned in these techniques can be easily transferred/applied to other similar layered 2D materials. Although previously overshadowed by graphene to some degree, graphene-analogous 2D materials have very peculiar, yet favorable, properties associated with their low dimensionality. In particular, transition metal dichalcogenides (TMDCs) show a wide range of electronic, optical, mechanical, chemical and thermal properties that could be useful in myriad of applications. There is at present a resurgence of scientific and engineering interest in TMDCs because of recent advances in mechanical exfoliation, transfer of 2D materials, and general physical understanding of 2D materials due to graphene.

1.3 Transition Metal Dichalcogenides

TMDCs are a class of 2D material with the chemical formula MX_2, where M is a transition metal element from group IV (Ti, Zr, etc.), group V (V, Ta, etc.) or group VI (Mo, W, etc.) and X is a chalcogen element (S, Se, Te). These materials form a layered structure of repeating X-M-X sandwiches, with the chalcogen atoms in two hexagonal planes separated by a plane of metal atoms (Fig. 1.4a). Adjacent sandwich layers are separated by van der Waals forces to form bulk crystals of various polytypes, depending on the coordination of M atoms within a single unit cell and the stacking order of the X-M-X sandwiches. Polytypes are different structures of the material with the same chemical composition. The most common polytypes in TaS_2 are the 1T, 2H and 3R (single-layered trigonal, double-layered hexagonal and triple-layered rhombohedral respectively) structures. The number specifies the stacking periodicity—crystal structure repeats every one, two or three layers in the c-axis (direction perpendicular to the layers). The trailing letter specifies the type of symmetry formed by the projection of atoms from the top view (Fig. 1.4b).

This class of layered 2D materials, unlike graphene, intrinsically comes with

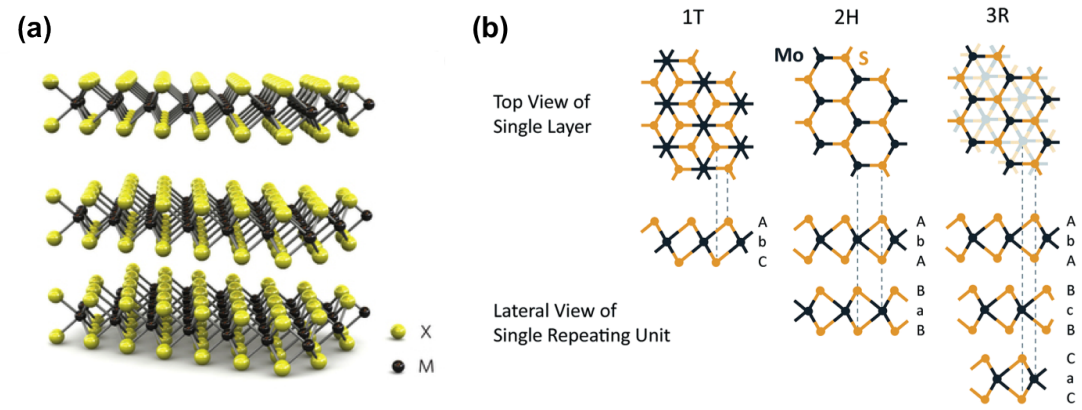

Figure 1.4: (a) Stick and ball diagram depicting the X-M-X sandwich layers separated by van der Waals force [10]. (b) Schematic crystal structures of the three polytypes 1T, 2H, and 3R. The dashed lines show how the top views and the lateral views match with each other [11].

a wide variety of bandgaps, ranging from metallic to direct/indirect bandgap of several eVs. With a wide variety of bandgap energy available, these 2D materials could be seamlessly harnessed in many diverse optical and electronic applications, without the need for any bandgap engineering. However, in order for these materials to infiltrate these applications, we need to not only solve growth and process integration issues (large-scale growth, material handling/transfer, etc.) but also garner a better fundamental understanding of these materials. These materials, due to their low dimensionality, exhibit very intriguing electronic behavior. One such behavior is the existence of a charge density wave (CDW), which is illustrated in greater detail in Section 1.5. Prior to understanding these phenomena, we need to recognize various growth techniques available in order to study these materials and realize potential applications.

1.4 TMDC Growth Techniques

Large-area, scalable thin-film growth of these materials is critical to not only many electronic, optical device applications but also for fundamental scientific research of materials.

Outside of the realm of electronic and optical application, the majority of the research on these materials were and are conducted on bulk, 3D material (many layers of X-M-X atomic layers separated by van der Waals force). In the last few years, as the interest in atomically thin layers of these materials continue to spike, researchers have begun adopting similar exfoliation strategies pertaining to graphene. Many recent works have included attempts to produce TMDC layers via chemical [12] and mechanical [13] exfoliation. However, these exfoliation methods yield TMDC atomic layers with a very modest footprint and give rise to large variability in layer numbers; rigorous control of mono-layer thickness still remains a challenge with such physical and chemical exfoliation methods. These exfoliation strategies will certainly be futile in the development of scalable, commercial opto-electronic devices. Hence, it is of critical need to develop large-area synthesis of mono-layer TMDC that is compatible with current semiconductor process techniques.

1.4.1 Thin Film Growth

Over the last few years, significant efforts have been devoted to the development of reliable, large-scale thin-film synthesis methods. One such method is the direct sulfurization of thin film of metal on SiO_2 (Fig. 1.5a), which was developed in 2012 [14]. This allowed for ready utilization of as-prepared samples for further device fabrication, without the need for any transfer steps. Growth of MoS_2 was demonstrated by first depositing a thin layer of Mo (1-5 nm) on SiO_2 by e-beam evaporation. Sulfur was then sublimed upstream in a tube furnace and carried by N_2 to the SiO_2 substrate placed downstream. At 750 °C, S reacts with Mo to form MoS_2. Even though the thickness of the MoS_2 grown directly relates to the thickness of the pre-deposited Mo metal, areas of various layer thicknesses were observed, as shown by the BF-TEM image in Fig. 1.5c. Another major limitation of this method is the poly-crystallinity of the grown material. The ring-like diffraction pattern in Fig. 1.5b shows evidence of the film being highly

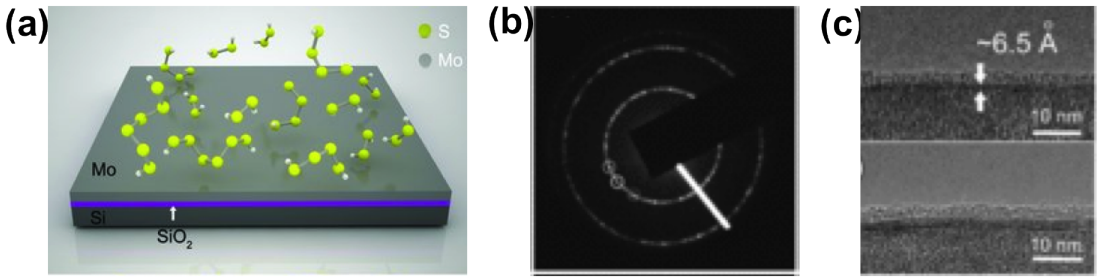

Figure 1.5: (a) Schematic representation of thin film of pre-deposited Mo on SiO_2 and sulfur gas flow. (b) Circular diffraction pattern shows rotational dissymmetry and poly-crystalline quality of film. (c) TEM image showing two and three layer MoS_2 [14].

poly-crystalline. With many nano meter sized crystal domains, the densely located grain boundaries will serve as scattering sites and limit the performance of the fabricated devices.

Since the previously described technique yielded TMDC films of low-crystalline quality, groups began searching for alternate synthesis schemes that could allow for larger grain sizes and higher crystallinity. A two-step thermolysis process was reported in 2012, which allowed for highly crystalline and large-area MoS_2 thin films on a variety of substrates [15]. The precursor $(NH_4)_2MoS_4$ was dip-coated on SiO_2/sapphire substrates followed by a two-step anneal (Fig. 1.6a). The first low-temperature anneal in H_2 atmosphere prevented oxidation that could compromise the quality of the growth. The second high-temperature anneal in Ar or Ar+S atmosphere improved the crystallinity of the film. A single anneal step with just H_2 gas flow was not possible since MoS_2 decomposes in the presence of H_2 at temperatures higher than 500 °C. The Raman spectroscopy measurement shows the quality of the film improving significantly after each anneal steps (Fig. 1.6b). The intensity of the Raman peaks increases and the E^1_{2g} peak width decreases notably after the second anneal step.

The devices fabricated with these MoS_2 layers in a bottom gate geometry exhibit n-type behavior with on/off current ratio of 10^5 and field-effect electron mobility up to 6 $cm^2/(V\ s)$, comparable with mechanically exfoliated MoS_2 on SiO_2.

The atomically thin layers grown in both the above methods do not exhibit

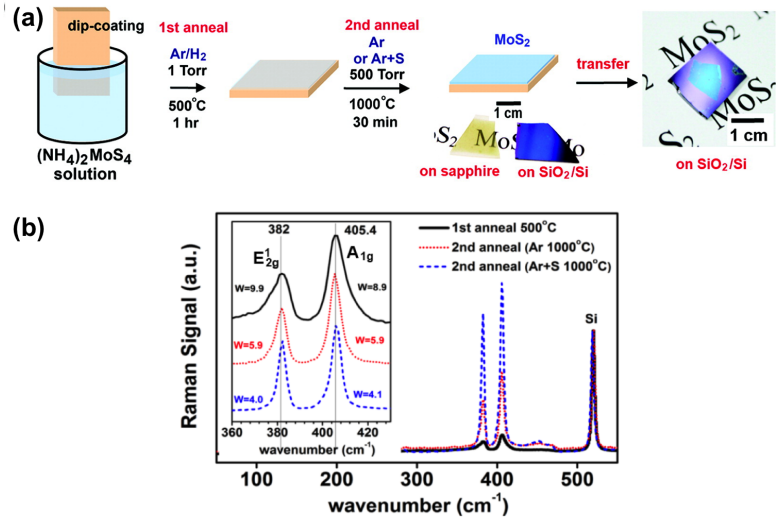

Figure 1.6: (a) Schematic representation of the two-step anneal process. (b) Raman spectroscopy of grown MoS_2 at various stages of the growth process [15].

any long-range order and poly-crystalline in nature. In order to improve the performance of device fabricated by these materials, we are in need of a novel epitaxial synthesis route, which could provide significantly larger domain sizes and lesser grain boundaries and defects. One such method was demonstrated by growing MoS_2 on an inert and nearly lattice-matching mica substrate by using low-pressure chemical vapor deposition. The growth is proposed to be mediated by van der Waals epitaxy between the MoS_2 and Fluorophlogopite Mica ($KMg_3AlSi_3O_{10}F_2$) [16]. The matching lattice symmetry (~2.7% lattice mismatch) between fluorophlogopite mica and MoS_2 was exploited for the epitaxial growth of monolayer MoS_2 on mica. Figure 1.7 shows the surface reaction during the epitaxial MoS_2 on mica substrate. MoO_3 was partially reduced by sulfur vapor to form volatile MoO_{3-x} species, which are then carried downstream by Ar carrier gas, adsorbed on mica, diffusing on the surface and reacting with sulfur to form MoS_2 layers.

$$S_2 + MoO_3 \longrightarrow MoS_2 + SO_2$$

This method allows for high-quality, uniform monolayer growth with very gentle

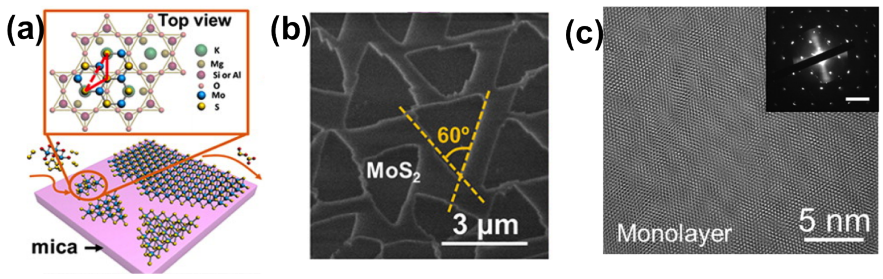

Figure 1.7: (a) Schematic representation of surface reaction during epitaxial growth of MoS_2 on mica. (b) SEM image showing initial growth of MoS_2 and relatively low nucleation density. (c) High-resolution TEM image of monolayer MoS_2. The inset shows a single diffraction pattern with six-fold symmetry, providing evidence for high crystallinity of the film [16].

and facile control of growth parameters. The van der Waals epitaxial growth with the slightly mismatched substrate gives rise to Stranski-Krastanov (layer-plus-island) growth with the critical layer number of 1 [16]. This newfound ability of achieving long-range crystal order and uniform layer control will prove crucial in the development of next-generation electronics and opto-electronic applications using these 2D materials.

1.4.2 Bulk Growth

The quest for uniform, crystalline, single-layer thin-film growth is still in its infancy and will undoubtedly be pivotal in the realization of next-generation, commercially viable devices. However, one should also realize large-scale, thin-film synthesis route is not the only route for preparing these materials. Many traditional methods for bulk growth of these materials have been in existence for many decades. These bulk synthesis method can be useful for many non-electronic applications, but more importantly, they can be valuable for fundamental research of these layered materials. These bulk growth techniques are more mature than the recently developed thin-film growth. This, along with some exfoliation technique, could provide a quick and effortless way to grow and study these layered materials, even down to a single or few layers.

The traditional method used to prepare these compounds involves the direct reaction of the elements in an evacuated quartz tube at elevated temperatures [17,18]. Poly-crystalline powder of TMDC can be synthesized by solid-state reaction of elemental transitional metal and chalcogen powder; the following reaction occurs by adding stoichiometric ratios of the metal (M) and chalcogen (X) powders.

$$\mathrm{M(s)} + 2\,\mathrm{X(s)} \longrightarrow \mathrm{MX_2(s)}$$

The evacuated quartz tube provides an ambient, void of any moisture or oxygen, and prevents any unwanted reaction/by-products. Also, in order to prevent any excess metal atoms intercalating between the layers, it is vital to have a slight excess of sulfur powder [19]. Although this is a slow reaction—growth time is typically in the order of days—this technique provides a simple solution to synthesize bulk poly-crystalline TMDCs.

However, at times, poly-crystalline material might not be sufficient for certain applications and/or studies; some applications/studies might require large-area bulk single-crystal material without any grain boundaries. A commonly used strategy to form single-crystals is chemical vapor transport (CVT). Solid-state researchers have used this method for over a century to synthesize various inorganic minerals. The historical roots of this synthetic method date back to the mid-19th century, when several observations on the formation of minerals in nature have been published. The formation of hematite in the presence of hydrogen chloride in the effluent of volcanoes is a naturally occurring CVT process, which is popularly known to have served as an inspiration for the first laboratory work on CVT [20].

Single-crystals of TMDC can be formed when an evacuated ampule containing only poly-crystalline TMDC and Iodine (I_2) is placed in a temperature gradient (Fig. 1.8). In this setup, the I_2 convection current serves as the transport agent for CVT-assisted growth. During CVT, the poly-crystalline charge of TMDC is first volatilized to a chemical intermediate phase at the higher-temperature end

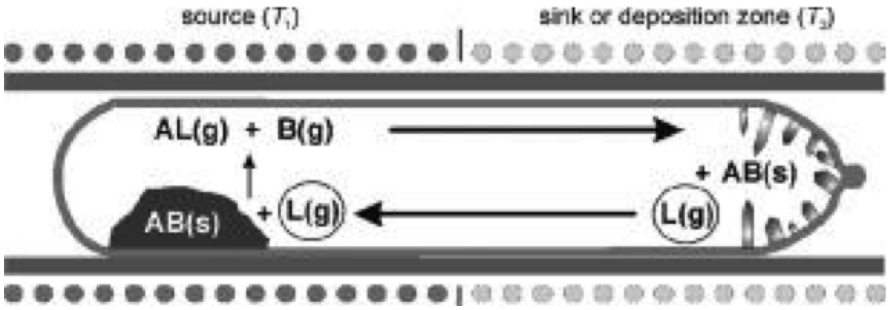

Figure 1.8: Sketch of a transport ampule in the temperature gradient of a two-zone tube furnace [20].

(T_1), as described in the following equation:

$$2\,MX_2(s) + 2\,I_2(g) \rightleftharpoons 2\,MI_2(g) + 2\,X_2(g)$$

Since an abundant amount of the TMDC source is present at the hotter end, the forward reaction is favored and the intermediate iodide is transported to the cooler end by an I_2 convection current. In the cooler end the following reversible reaction occurs:

$$2\,MI_2(g) + 2\,X_2(g) \rightleftharpoons MI_4(g) + MX_2(s) + X_2(g)$$

At the growth temperature dissociation of di-iodide to tetra-iodide occurs, giving rise to nucleation and crystal growth of TMDC. A very small amount of iodine is required for this CVT growth since the iodine gas is constantly recycled.

Although the primary scope of this thesis is TMDC, an important caveat to note is that not all material systems entail the initial reaction to occur at the hotter end and the growth reaction to occur at the cooler end. Depending on the thermodynamics of the forward reactions (exothermic or endothermic), the growth and initial reaction temperatures might be reversed for CVT growth of a different material [20].

Armed with various thin-film and bulk material TMDC growth strategies, we can synthesize various types of TMDCs and pave the way for further investigation

of the material; with appropriate exfoliation techniques, we can even exploit the relatively simpler bulk growth strategies to investigate atomically thin sheets of these materials.

1.5 Charge Density Wave in TMDCs

The low dimensionality of these materials gives rise to many peculiar properties that are worth investigating. One such unusual property is the existence of charge density wave (CDW). Unlike bulk material, lattice distortion in some of these low-dimensional materials create CDWs, which gives rise to non-uniform, wave-like electron densities.

1.5.1 Fundamental Theory of CDW

CDW systems have been an area of research in the condensed matter community for many years now. This phenomenon was first predicted by Peierls in the 1950s and first observed in the 1970s. Since then, CDWs were observed in various inorganic low-dimensional materials, such as TMDCs and transitional metal trichalcogenides. In order to fully realize the origin of CDWs, we will begin by examining a simpler periodic 1D chain of metal atoms. This will illustrate the transition into the CDW state and how it is connected with a periodic structural distortion, caused by a partial opening of the Fermi surface.

Let us first assume a periodic 1D chain of metallic atoms, separated by atomic spacing of $\mathbf{a}$. By just assuming nearest neighbor interaction, we can arrive at the dispersion relationship shown in Fig. 1.9a. The first Brillouin zone in the k-space extends from $-\pi/\mathbf{a}$ to $\pi/\mathbf{a}$ and the Fermi level sits at $\mathbf{E_F}$ and $\mathbf{k_F}$. This results in a half-filled band, where all energy levels above the Fermi level remain empty. Now, let us imagine the atomic lattice to be distorted by $-\pi/\mathbf{k_F}$. This causes the Brillouin zone boundary to move to the point where the last filled state is $\mathbf{k_F}$. This process opens up a gap at the Fermi energy, where the filled states go

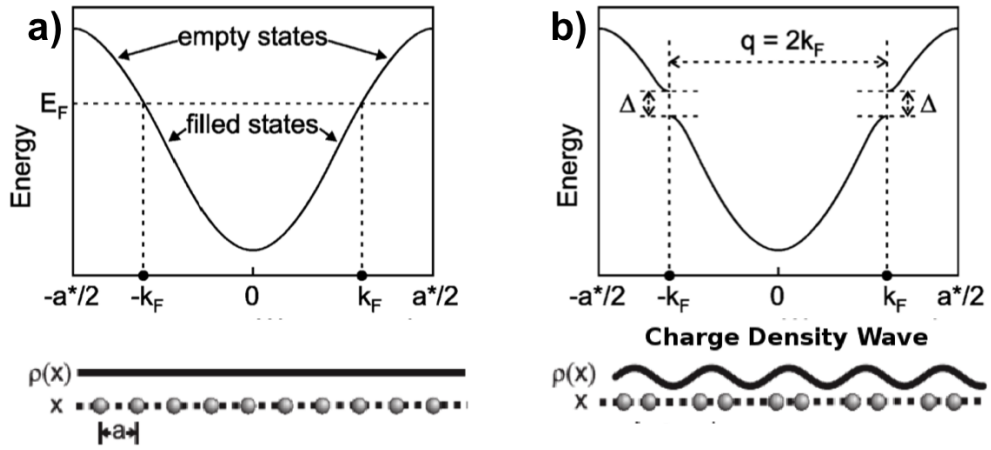

Figure 1.9: A quasi-1D metal, as shown in (a) can reduce its energy by undergoing a periodic lattice distortion and developing a CDW, as shown in (b) [21].

to a lower energy and the empty ones to a higher energy, as seen in Fig. 1.9b. Therefore, this lattice distortion becomes energetically favorable, if and only if the energy savings from the new bandgap outweighs the elastic energy cost to strain the lattice. The energy cost is minimized when the atomic vibration/thermal excitation is minimized (i.e. the lower the temperature, the lower the energy cost). Hence, at temperatures lower than some critical temperature, T_{CDW}, we begin seeing the manifestation of lattice distortion and charge density waves.

One should also be aware that CDWs can be commensurate or incommensurate with the underlying lattice. For example, in a crystal with exactly a half-filled band, the CDW state corresponds to a periodic structure with a spacing that is twice as large as the periodicity of the original structure. In general however, the filling of the conduction band is not related to the lattice periodicity of the crystal and the CDW super-lattice periodicity can take on any value. If the CDW super-lattice constant is an integer multiple of the lattice constant **a**, the CDW is said to be in a commensurate phase. In contrast, the CDW is incommensurate if the ratio of the super-lattice periodicity and the atomic lattice periodicity is an irrational fraction.

1.5.2 CDW in 1T-TaS_2

Among the many TMDC compounds, 1T-TaS_2 (1T polytype of tantalum (IV) sulfide) exhibits one of the most complex and intriguing CDW behaviors. Conveniently, this material also has a high T_{CDW} temperature. Since the T_{CDW} temperature occurs at temperatures higher than the room-temperature, 1T-TaS_2 serves as an ideal candidate for room-temperature, ultra-high vacuum-scanning tunneling microscopy (UHV-STM) CDW study. This greatly simplifies the experimental setup and eliminates the need for external cooling of the substrate; active cooling of the sample within a UHV scanning tunneling microscope system is non-trivial and will require intricate system modification. The details of this UHV-STM study will be presented in Chapter 3.

At high temperatures 1T-TaS_2 is metallic; however, upon cooling below 543 K 1T-TaS_2 exhibits three main temperature-dependent CDW phases—commensurate, nearly commensurate and incommensurate [22]. The temperature-dependent phase change is illustrated in Fig. 1.10.

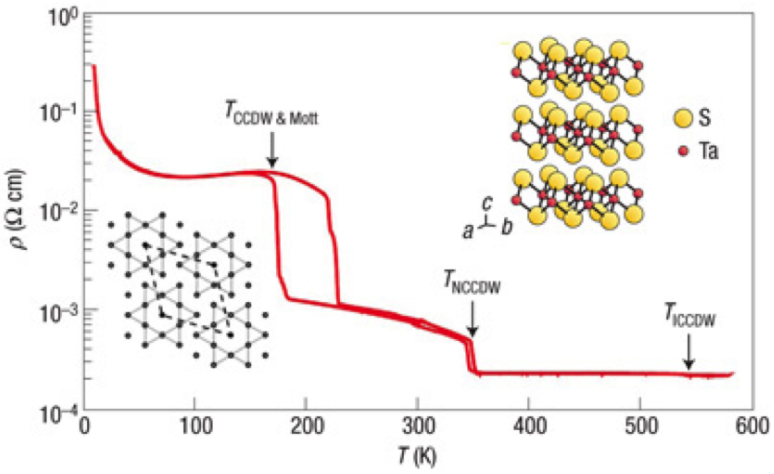

Figure 1.10: Temperature-dependent resistivity measurement illustrates the three distinct CDW phases present in 1T-TaS_2. Inset shows the a, b and c axes of the crystal and an illustration of the commensurate CDW phase [22].

At high temperatures, close to T_{CDW}, the CDW is incommensurate relative to the atomic lattice. For T < 183, the CDW goes through a phase transition and rotates 13.9° relative to the atomic lattice to become commensurate (Fig. 1.11a).

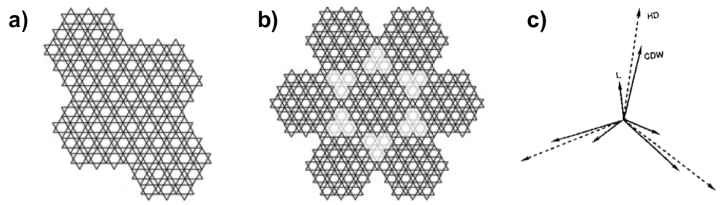

Figure 1.11: (a) Schematic top view of the commensurate CDW phase compromising of interlocking Star of David pattern [22]. (b) Schematic top view of the nearly commensurate phase at 300 K, depicting the larger hexagonal superstructure within the CDW lattice [22]. (c) Vectors representing the relative orientation of the hexagonal domains, the CDW and atomic lattice [23].

In the intermediate temperature, the CDW phase appears to be neither entirely commensurate nor entirely incommensurate. The nearly commensurate phase adopts a novel, hexagonal domain-like structure, where there is an additional periodic variation in the CDW amplitude that occurs on a wavelengths larger than the fundamental CDW wavelength (Fig. 1.11b and c). The CDW exhibits a fascinating hierarchy of structures: the hexagonal atomic lattice with a period of 3.35 Å, the fundamental CDW lattice with a period of 12 Å and the hexagonal super-lattice with period 70 Å [23].

CHAPTER 2

GROWTH OF 1T-TANTALUM (IV) SULFIDE

In this chapter, prior to dwelling into the STM study of the material and its CDW properties, we will present the growth strategies and the experimental setups required for the successful synthesis of 1T-TaS_2. As discussed in Chapter 1 (Section 1.4), a large assortment of thin-film and bulk growth strategies is available for the growth of 1T-Ta_2. We need to evaluate these different strategies and wisely select the most cost-effective and reliable solution to satisfy our material needs.

The primary focus of this thesis involves the study of CDW in 1T-TaS_2 via UHV-STM. Since we were not targeting any scalable, potential commercial application, a large-area, scalable thin-film growth was not of high importance. Thin-film growth techniques are still in active development and require careful control and nuance to give high yielding growth. Although we intend on studying monolayer and few-layer 1T-TaS_2, with an appropriate exfoliation strategy however, we can exploit the simpler bulk growth strategy to synthesize the material of interest.

2.1 Direct Synthesis of Poly-Crystalline 1T-TaS_2

In this section, we will examine the growth setup and recipe required for the synthesis of poly-crystalline 1T-TaS_2 in greater detail. Synthesis requires the direct reaction of the elements in an evacuated ampule at elevated temperatures; stoichiometric ratio of elemental metal (Ta) and chalcogen (S) powder were sealed within an evacuated quartz tube and heated to the desired temperature in a furnace.

2.1.1 Quartz Ampule Preparation

Since the anneal temperature required to form the 1T polytype of TaS_2 is close to 1000 °C, the reaction ampule needs to withstand prolonged high temperatures. Silica or pure quartz (SiO_2), the purest of silica-based glasses, has an annealing temperature of 1100 °C. Although silica's high working temperature and brittleness limits application, its durability at high temperature makes it a useful material for many high temperature processes. Also, at temperatures above 1200 °C, silica begins to move under its own weight and deform with a cloudy appearance, before starting to melt at close to 1650 °C. Since 1200 °C is well above our operating temperature but low enough to allow for the flowing of quartz to form a seal with an oxy-hyrdogen flame, pure silica makes for an excellent material for our reaction ampule.

An important aspect of the growth involves the sealing of reagents under a vacuum. This requires the quartz tube geometry, mainly its outer diameter, to be compatible with compression fittings that are commonly used in vacuum systems. 12.7 mm (0.5 in.) outer diameter fused silica tubes with wall thicknesses of 1 mm and lengths of 4 feet were obtained from Alfa Aesar (product number 42276). The tubing was then cleaved to different lengths depending on the type of growth. For the poly crystalline powder synthesis, the tubes were scribed to 8-9 inches. For CVT growth of single-crystal 1T-TaS_2, the ampules were trimmed to a larger size in order to fit the two-zone furnace configuration (see Section 2.2).

Upon scribing and snipping the quartz tubing to the appropriate length, one end of the tubing was closed off using an oxy-hyrdogen flame. Combustion of a mixture of hydrogen (H_2) and oxygen (O_2) gas produces a high-temperature flame at the nozzle of the oxy-hydrogen torch. A maximum temperature of 2800 °C is achieved with an exact stoichiometric ratio of 2:1 (H_2:O_2), which is much greater than the melting point of fused silica. Different sized flames of various strength can be created by simply adjusting the hydrogen and oxygen flow rates. To complete this procedure, one end of the open ended quartz tube was first

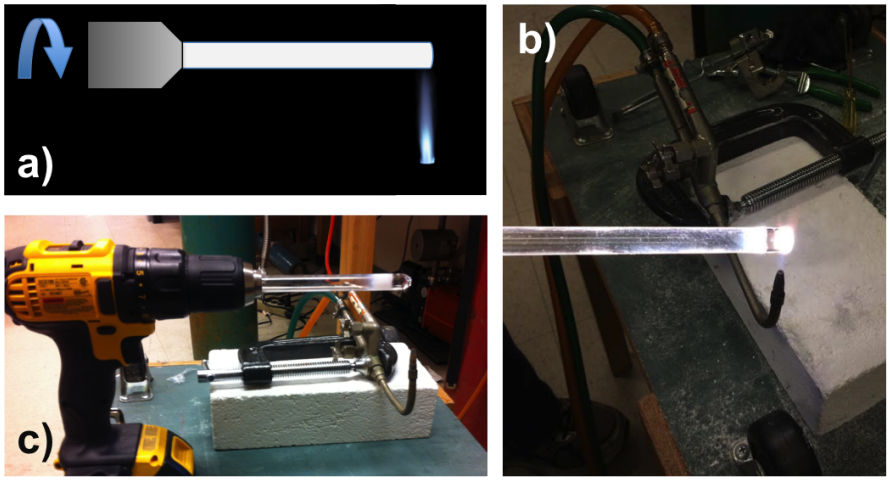

Figure 2.1: (a) Schematic view illustrating the sealing of the quartz tube using an oxy-hydrogen flame and hand drill. (b) Quartz tube beginning to glow white-hot upon heating. (c) Fully formed seal using oxy-hydrogen flame. Tube is now ready for flame anneal and precursor loading.

wrapped in aluminum foil and attached to a power drill. The aluminum foil not only helps conduct heat away quickly from the drill chuck, it also serves as a soft, protective layer when the chuck is pressed tightly onto the tube. The tube is then slowly revolved, with the end further away from the chuck directly over the flame (as show in Figure 2.1).

After one end of the quartz tube is sealed, we load the elemental precursors, Ta and S powder, into the tube. Prior to precursor loading, the tubes were hydrogen flame annealed to remove any excess moisture or impurities that are physisorbed on the quartz tubing. Stoichiometric ratios of Ta and S powders were measured using a sensitive digital mass balance to give approximately 1 g of total charge. Using a clean stainless steel spatula, 0.738 g of Ta (atomic mass = 180.948 g/mol) and 0.267 g (5 mg in excess) of S powder (atomic mass = 32.065 g/mol) were measured and loaded into the quartz ampule—having excess S prevents intercalation of Ta within the van der Waal's gap, as explained in Section 1.4. Careful attention was taken to ensure the powder was dropped directly to the bottom of the ampule without sticking to the sides of the ampules; the precursors, especially sulfur, with a high room-temperature vapor pressure, should be as far

away as possible from the top of the tube. The reason for this will be elucidated in Section 2.1.3.

2.1.2 Turbo Station Setup

Once the precursors have been loaded into the growth ampule, the quartz tube is then connected to a vacuum pump and evacuated. This involves pumping out the tube down to around 1E-4 Torr using a turbomolecular (turbo) pump, backed by a roughing pump. The roughing pump performs two distinct functions to support the high-vacuum turbo pump. The roughing pump first rough pumps the vacuum chamber from atmospheric pressure to low enough pressure to allow the turbo pump to operate, and then performs its secondary function of supporting the turbo pump by providing a low enough foreline pressure at the turbo pump's exhaust. Firstly, the pump's inlet pressure (chamber pressure) needs to be low enough that rotors of the turbo pump can pump out the residual gas molecules. These molecules are compressed through the pump and exhausted at some other reduced foreline/exhaust pressure where the supporting roughing pump exhausts them from the system. The roughing pump ensures that the foreline/exhaust pressure is below its maximum pressure limit, allowing the turbopump to operate at its rated efficiency. The roughing and turbo pumps are attached to a multi-functional, stainless steel UHV chamber, which is used for various experiments within the Lyding group. A simple modification was done to interface the turbo station with the quartz ampule. One of the blank CF (ConFlat) flanges connected to the turbo station was removed and replaced with a flexible stainless steel hose with CF flange fittings at both ends. At the heart of the CF flange is a knife-edge that is machined below the flange's flat surface. As the bolts of a flange-pair are tightened, the knife edges make annular grooves on each side of a soft copper gasket. The malleable copper gasket then fills all the machining marks and surface defects in the flange, yielding a leak-tight seal. Although these CF seals are common place in many stainless steel UHV chambers, they do not interface

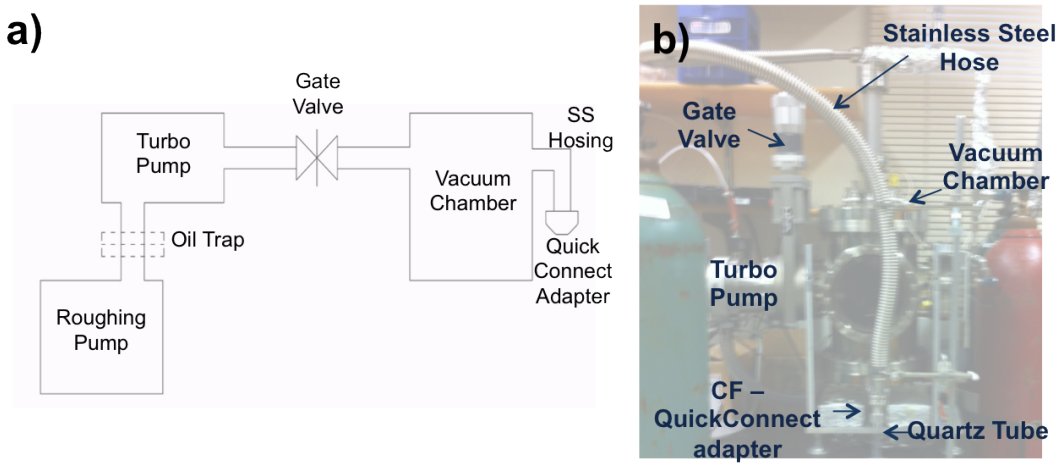

Figure 2.2: (a) Schematic view of the vacuum system. (b) Actual image of the system with the various components labeled. (The roughing pump is not in view in this image.)

well with the brittle quartz tubes. Hence, a CF to Quick-Connect adapter was attached to the end of the stainless steel hose to form a tight seal around the loaded quartz ampule; with the aid of a Viton® gasket, the Quick-Connect fitting provides an easy, quick and reusable seal. Figures 2.2 a) and b) show a schematic and physical representation of the setup respectively.

2.1.3 Ampule Evacuation and Seal

Using the modified turbo station setup, the single-ended quartz tube is evacuated to the desired pressure as measured by thermocouple and cold-cathode gauges. Throughout the evacuation and seal phase, the bottom end of the quartz tube is submerged in liquid N_2. The reason for this is the large vapor pressure of sulfur at room-temperature. Sulfur tends to volatilize readily and needs to be cooled to cryogenic temperature to ensure that the sulfur precursor is not lost during this phase. The length of the tube is carefully selected such that the point of constriction is spaced far away from the bottom end of the tube (to ensure that the S powder is submerged in L-N_2 and kept cool) and spaced far from the top end of the tube (to protect the Viton® gasket from the high-temperature flame),

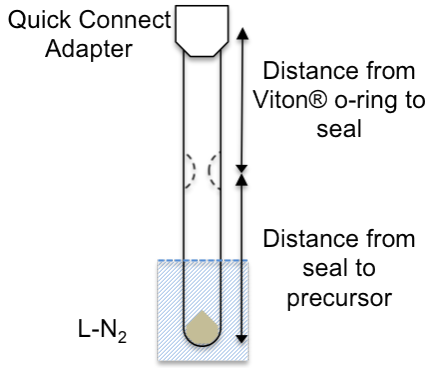

Figure 2.3: We need to ensure adequate distance exists between the seal and Viton® gasket in order to protect the gasket from the high-temperature flame and ensure a long gasket lifetime. Also, there should be ample distance between the precursor and the seal to ensure the sulfur powder remains in the ampule during the high-temperature sealing process.

as illustrated in Fig. 2.3. During the evacuation phase, the quartz tube is first evacuated to ∼1E-1 Torr using the roughing pump alone and then to ∼1E-4 Torr using the turbo and roughing pump. Once evacuated, the tube is sealed using an oxy-hydrogen flame to give an evacuated quartz ampule with the necessary precursor for the growth of poly-crystalline 1T-TaS_2.

The sealing of the relatively large diameter (outer diameter = 0.5 in.) using an oxy-hydrogen flame is a non-trivial task even for an experienced glassworker. Due to the vacuum within the tube and uneven heating from the oxy-hydrogen torch, the sidewalls rapidly collapse and causing the quartz to implode. Most implosion occurs close to the narrow constriction/seal; The outer diameter/inner diameter ratio is greatest at this point—allowing the outer wall to invade the inner diameter at a greater depth, which thins and weakens the sidewalls leading to implosion. Figure 2.4 shows an example of an unsuccessful attempt at sealing the tube. This problem could be mitigated through various means. One solution will require a redesign of the nozzle to deliver a circular, ring-like flame that could provide more even heating. With uniform heating, the sidewalls will collapse uniformly and avoid implosion. Although such intricate nozzles are available commercially, we searched for a more inexpensive solution. An alternate solution, with no

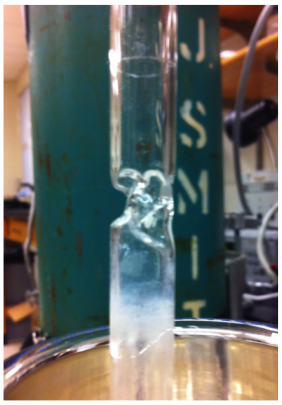

Figure 2.4: An unsuccessful attempt at sealing the tube. The quartz tube punctured near the constriction during the seal and breaking vacuum.

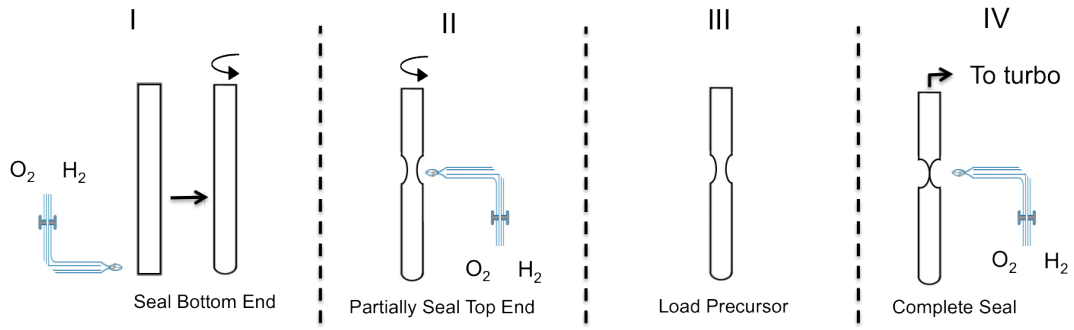

Figure 2.5: Schematic representation of the pre-growth process flow, illustrating quartz tube preparation (I), partial constriction of tube (II), precursor loading (III) evacuation and seal (IV).

system redesign or additional cost, was to form a partial seal prior to precursor loading. Figure 2.5 shows a schematic illustration of the new process flow. Partial constriction of the tube prior to evacuation is an easier task that constricting the tube during evacuation. Since the tube is void of any volatile precursor and is not directly connected to any fixed vacuum fitting, we can now evenly heat the tube by connecting the tube to a hand drill, similar to the initial sealing of the bottom end of the tube. The tube is held vertically and rotated adjacent to a horizontally pointed flame as shown in Fig. 2.5; if the tube was rotated around a different axis, gravity causes the tube to bend as soon as the quartz begins to flow. Figure 2.6 shows a zoomed-in image of the constriction made during a typical partial-seal.

The outer diameter around this newly made constriction range from 3.5 mm to

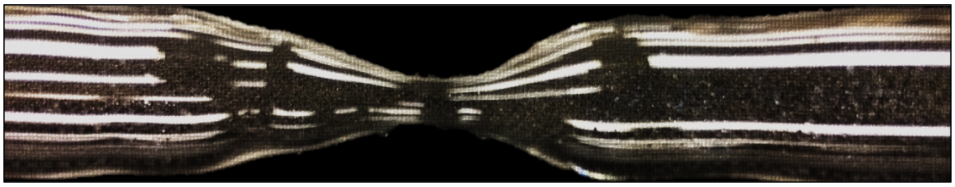

Figure 2.6: Example image of a partially sealed tube. The outer diameter at the constriction is 3.5mm.

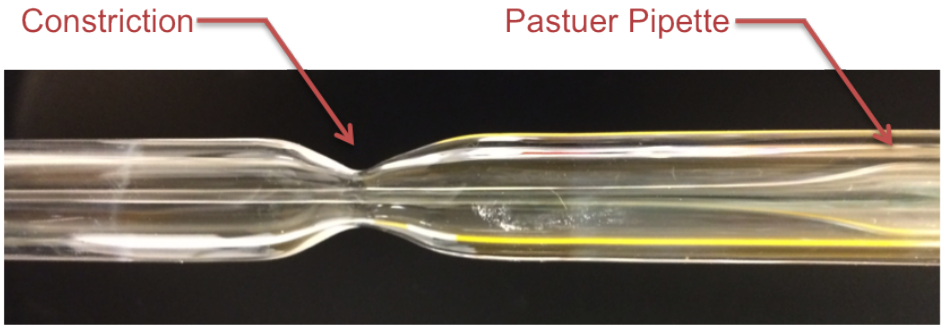

Figure 2.7: Image of Pasteur pipette and partially sealed quartz tube. The neck of the pipette extends below the constriction.

7 mm, significantly lower than the initial outer diameter of 12.7 mm. The smaller diameter greatly reduces the complexity of successfully completing the seal, even with irregular heating from the traditional nozzle/flame. The only disadvantage of this partial-seal method is that additional measures need to be taken during the loading of precursor; we can no longer deposit the elemental precursor directly to the bottom of the tube, through the narrow constriction. A glass Pasteur pipette with a long neck was used to bypass the constriction and deposit the precursor directly to bottom of the tube, as shown in Fig. 2.7.

2.1.4 High Temperature Growth

Once the ampule is evacuated and sealed, it is placed inside a tube furnace. All growths were carried out using a Marshall (1000 Series) Furnace, a two-zone, shunt-type horizontal tubular furnace with a heating element consisting of a heavy gauge Nickel-Chrome wire wrapped around a ceramic tube. The shunt-type furnace, with a maximum temperature rating of 1100 °C, has a number of external

"taps" or "shunts" incorporated into the element winding in addition to the normal power feed taps. By placing a suitable length of resistance wire from one shunt tap to another, a parallel shunt resistance is created, thereby reducing the amount of local current through the winding between the shunt taps; the external resistor effectively lowers the temperature of the regions that have been shunted. With proper shunt selection and placement, a more uniform and longer uniform temperature zone can be achieved.

By placing the quartz ampule in the middle of one of the zones, the growth was carried out using a single-zone configuration. Since the dimension of the quartz ampule was comparable to the shunt tap distance, the shunt taps were left open—no additional or useful temperature control can be achieved by current shunting. A control run without any quartz ampule showed adequate temperature uniformity along the length scale of interest. The growth was carried out by ramping the temperature of the furnace to the growth temperature of 975 °C and the growth was carried out for 3-7 days. The proportional-integral-derivative (PID) controller settings (Rate, Reset, Proportional Band) were set such that the manual ramp to the set-point temperature, took anywhere between 3.5 hours to 4 hours. Since the initial reaction is highly exothermic and sudden changes in internal pressure could lead to an explosion of the ampule [24], a slow ramp rate was selected. The growth temperature of 975 °C was chose since the 1T polytype of TaS_2 only exists stably at temperatures above 850 °C.

2.1.5 Post-Growth Quench

At the end of the growth, the evacuated quartz ampule is removed from the furnace. Before the temperature drops below 850 °C, the quartz ampule is quenched in a 50% water 50% ice bath. This rapidly cools the TaS_2 powder and locks it in its metastable 1T crystallographic phase. In the absence of a quench, the material has enough energy to revert to its room-temperature stable 2H polytype. Even though the 2H polytype exhibits charge density wave behavior, it has a much

lower T_{CDW} temperature and making it unsuitable for room-temperature study. Hence, it is of utmost importance to rapidly quench the reaction and capture the material's 1T phase.

After a 10 min quench, the ampule is taken out of the ice/water bath and is allowed to equilibrate to room-temperature. The quartz ampule can then be opened by scribing the ampule and snapping it in half. The ampule cleaves easily with an inward rush of air disturbing the lighter material near the opening. For safety reasons, this action was performed in a fume hood.

2.1.6 Anomalous Growth

The pure polycrystalline 1T-TaS_2 powder appears as a dark grey, free-flowing powder. In a typical growth, a complete reaction of the reagent gives poly-crystalline 1T-TaS_2 and the excess sulfur condenses on the sidewall and escapes out of the tube when cracked open, as shown in Fig. 2.8a. Figure 2.8b shows an image of the ampule after an atypical growth (an unknown amount of excess S was mistakenly added during precursor loading). After a three-day growth, along with the dark grey 1T-TaS_2, small flakes of single-crystal 1T-TaS_2 were observed near the bottom of the ampule. In Fig. 2.8b, we also notice a tinge of yellowish-green substance deposited on the sidewall, which could signify the presence of unreacted sulfur. A possible explanation for this growth could be that the excess sulfur gas acted as a carrier gas and assisted with a chemical vapor transport (CVT) growth of 1T-TaS_2 single-crystals. The experiment was repeated with a controlled amount of excess S (additional 5 mg) to confirm this hypothesis, but the controlled study did not yield any single-crystal 1T-TaS_2.

The reason for the anomalous growth of single-crystal 1T-TaS_2 remains unclear. Using this poly-crystalline growth method, reliably synthesizing single-crystal 1T-TaS_2 will prove difficult, unless the process conditions from the atypical growth are controllably repeated. Certain conditions such as temperature profile within the furnace can vary by a significant margin and cannot be systematically controlled

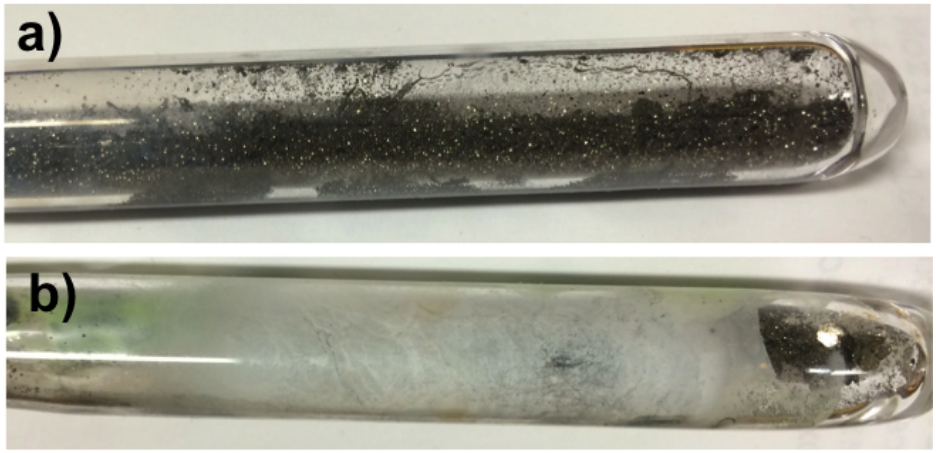

Figure 2.8: (a) Typical growth showing dark grey powder of poly-crystalline 1T-TaS_2. (b) Atypical growth with additional golden, single-crystal 1T-TaS_2 near the bottom of the ampule. A tinge of yellowish-green, possibly unreacted sulphur, is observed on one end of the ampule.

with a single-zone setup. Although, the single-zone setup serves as an adequate and reliable technique for poly-crystalline 1T-TaS_2 growth, a more systematic two-zone approach needs to developed for reliable single-crystal growth.

2.2 CVT Growth of Single-Crystal 1T-TaS_2 Using I_2 Vapor

As seen in Section 1.4.2, an important requirement for single-crystal growth using CVT is a temperature gradient. To achieve controllable temperature gradient, a two-zone tube furnace is required. Each of the zones should be powered independently using two separate controllers and the tube be placed at the boundary of the two zones.

In our setup, two independent Barber Coleman 570 series PID controllers are used to supply current to the furnace windings. All controller parameters, except the set-point temperature, are kept constant between the two controllers so that the ramp rate is similar for both controllers. Due to the difference in the furnace winding resistances between the two zones, the controller settings were empir-

ically adjusted to compensate for this difference and to obtain identical ramp rates. The reason for this resistance difference is highlighted in Appendix A. Before commencing the single-crystal growth experiments, the furnace needed some initial maintenance to restore its two-zone functionality. The details of the issue, diagnostic and fix are also presented in Appendix A.

The preparatory steps for CVT-assisted growth of single-crystals are similar to the poly-crystalline 1T-TaS_2 growth. The turbo station setup and quartz ampule preparation, including the partial constriction of the tube, are almost identical to one another. The only difference is the dimensions of the tube; the tube is cut to a longer dimension (13 inches instead of 9 inches) so that the tube is long enough to span across the two zones. Once the partial constriction is made, instead of loading the elemental precursors Ta and S, the previously made 1T-TaS_2 is dropped to the bottom of the ampule. Due to its granularity and free-flowing nature, the poly-crystalline 1T-TaS_2 was added directly to the ampule without the aid of any Pasteur pipettes. The large granules tend to get stuck within the thin, narrow Pasteur pipette neck and thereby hinder subsequent loading. Once 0.75 - 0.8 g of 1T-TaS_2 powder is measured and loaded, I_2 (transport agent) pellets are subsequently dropped to the bottom of the ampule. Only 5 mg/cm^3 of I_2 is needed since the iodine gets recycled again each forward cycle. By measuring the length of the ampule from the bottom to the constriction and using a perfect cylinder approximation, we calculate the required mass of I_2.

Following the addition of 1T-TaS_2 and I_2, the ampule is evacuated and sealed as detailed in Section 2.1.3. The growth was carried out in a two-zone furnace, with set-point temperatures of 880 °C and 950 °C. The end containing the poly-crystalline powder was positioned in the hot zone so that the endothermic growth reaction can occur at the cooler zone to form single-crystal 1T-TaS_2. A schematic of the furnace and the ampule is shown in Fig. 2.9. The P-I-D settings were set such that the ramp rates were uniform between the two zones. The ramp to 880 °C takes approximately 5 hours and it takes an additional 20 mins to climb from 880 °C to 950 °C. The furnace was left at the set-point temperature for 1 week for

the growth to complete. After a week of growth, the ampule is removed from the furnace and dropped into a 50% water 50% ice bath. As previously mentioned in Section 2.1.5, the rapid cooling locks the single-crystals in the 1T phase. After a 10 min quench, the ampule is allowed to equilibrate to room-temperature before scribing it open. The crystal flakes and any unreacted 1T-TaS_2 powder is removed by carefully shaking the ampule. Crystal flakes that adhered more strongly to the sidewalls were removed using a Teflon tweezers. The resulting crystals were gold in color as expected. The crystal flake dimensions ranged anywhere from 2 mm to 6 mm, as shown in Fig. 2.10.

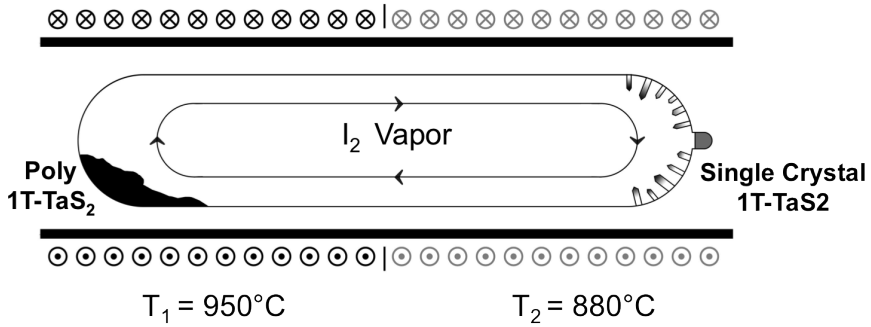

Figure 2.9: CVT growth of single-crystal 1T-TaS_2. The left zone with the poly-crystalline powder is set to 880 °C and the right zone, the growth zone, is set to 950 °C. The I_2 convection current carries the reagents and by-products form the source to the growth zone, and vice versa.

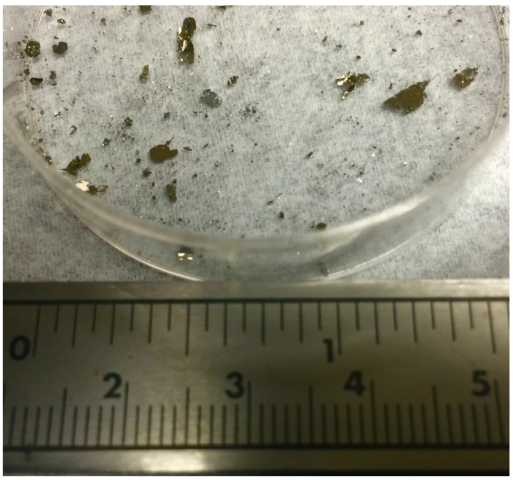

Figure 2.10: Image of grown crystal. Crystal dimensions are in the order of a few millimeters.

CHAPTER 3

STM STUDY OF 1T-TANTALUM (IV) SULFIDE

Following the development and success of the growth process flow, we focused our attention on characterizing the grown 1T-TaS_2 using Ultra-High Vacuum Scanning Tunneling Microscopy (UHV-STM). As discussed in Section 1.5, 1T-TaS_2 exhibits a room-temperature CDW phase, which can be visualized and characterized using by the STM.

3.1 Scanning Tunneling Microscopy

In 1982, Gerd Binnig and Heinrich Rohrer were the first to exploit the quantum mechanical phenomenon of electron tunneling to image atoms on a conducting surface [25]. A distinctively unique feature of the STM is its ability to probe both the electronic and topographic properties of the surface at the angstrom-scale, which can be harnessed for CDW studies of many materials. Since its invention, STM has not only been used as a microscopy tool but also to write atomic-scale patterns [26], study the barrier height of various material systems [27], and study superconductors and CDW materials [28, 29].

The underlying basis for the operation of the microscope is electron tunneling between an ultra-sharp metal tip and a conducting sample. When the tip and sample are brought sufficiently close using piezoelectric actuators, the electron wavefunctions in the tip and sample begin to overlap and a tunneling current is detected. If a bias voltage, V, is applied to the sample (tip is grounded relative to sample), a tunneling current, I, will flow between the sample and tip. If $V > 0$, electrons will tunnel from filled states in the tip to unfilled states in the sample.

Conversely, if V $<$ 0, electrons will tunnel from filled states in the sample to empty states in the tip. For a simple one-dimensional system, quantum mechanical treatment predicts an exponential decaying solution for the electron wave function in the barrier, as shown in Equation 3.1.

$$\Psi(d) = \Psi(0)e^{-\kappa d}, \text{ where } \kappa = \sqrt{2m(\Phi - E)}/\hbar \tag{3.1}$$

This strong exponential dependence of the tunneling current on distance enables very high vertical resolution. An atomic resolution map of the surface can be created by rastering an ultra-sharp tip over the surface using sensitive piezoelectric controls.

There are two main modes of operation for the STM: "constant height" scanning and "constant current" scanning. In the "constant height" scanning mode, the tip height and bias voltage are kept constant. Depending on the instantaneous tip-sample spacing during the raster scan, different tunneling current is detected throughout the scan. If the density of states is constant across the scanning surface, the change in current will directly correlate to the surface topography. In the "constant current" mode, feedback electronics adjusts the tip-sample spacing to maintain a user-defined reference tunneling current as the tip rasters across the scan area. By measuring the vertical displacements needed to maintain a constant current, one can obtain an image that indicates the spatial variation of the local density of states (LDOS) and surface atomic corrugation. All STM scans in this thesis were performed using the "constant current" mode. A diagram of a typical STM setup is show in Fig. 3.1.

All STM scans were performed under ultra-high vacuum (UHV). The entire multi-stage vacuum system is partitioned into three major chambers/stages: STM chamber, preparatory (prep) chamber and loadlock. The STM assembly itself is situated inside the STM chamber with a base pressure in the mid-10^{-11} Torr range. The UHV system provides a clean environment and prevents molecules in the air from contaminating the tip and sample surface. Also, the STM assembly is vi-

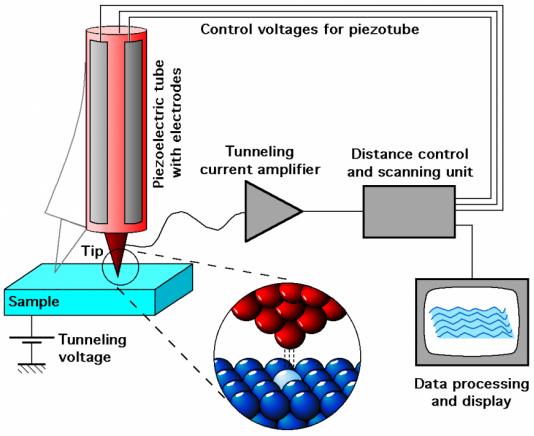

Figure 3.1: Schematic representation of an STM showing the tip, current amplifier and feedback loop. The tunneling current is maintained by the feedback loop as the tip rasters over the surface [30].

brationally isolated from its surrounding; this inhibits atomic-scale oscillation, which could prove detrimental for atomic resolution imaging. The STM chamber is isolated from the prep chamber by a UHV gate valve. All sample and tip preparation prior to scanning takes place within the prep chamber with a moderately higher base pressure of 1.1E-10 Torr. A dipstick, with electrical feedthrough, is located within the prep chamber to assist with sample and tip preparation. The prep chamber is also isolated from the loadlock (with a significantly larger base pressure) by another UHV gate valve. The isolation is important since the loadlock is used to transfer samples into and out of the UHV system and is regularly exposed to the ambient environment. The loadlock is normally maintained at a higher pressure (mid-10^{-8} Torr) by a turbo molecular pump, which is backed by a roughing pump. Another important component of the UHV system is the linear translation maipulator (LTM). These linear motion devices assist with the transfer of sample and tips between each of the previously mentioned vacuum chambers. The different vacuum environments are maintained by a combination of ionization pumps, turbomolecular pumps and roughing pumps. An illustrative model of the multi-stage vacuum chamber and the associated pumps are provided in Fig. 3.2.

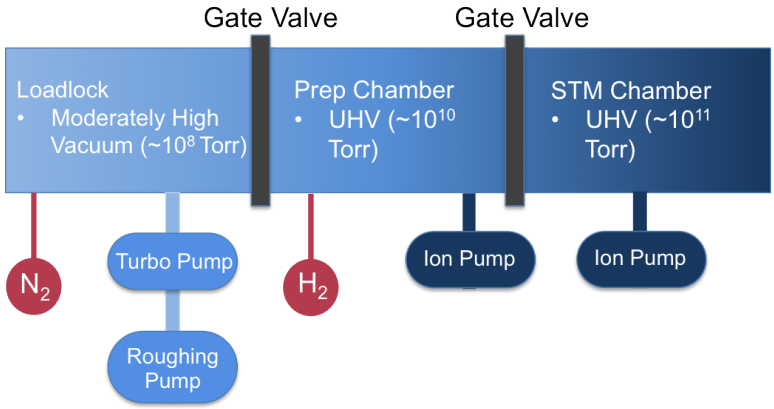

Figure 3.2: Schematic diagram of the multi-stage vacuum chamber, showing the base pressure in the different chambers. The diagram not only shows the pumps connected to the various chambers to achieve the necessary base pressure, it also shows the various gas supplies attached to chambers. Since this is a high-level diagram, not all vacuum valves are shown in this diagram.

3.2 Tip Preparation

The condition and sharpness of the tip will markedly influence the quality of the image data obtained; the radius of curvature at the tip apex strongly correlates with the lateral resolution achieved by the STM. If the apex of the tip terminates in a single atom, then majority of the tunneling current flows between the atom and nearby surface; due to the exponential dependence on distance, atoms adjacent to the apex barely contribute to the tunneling current. Hence, tip preparation plays a crucial role in any STM study. In this study, most of the tips used were fabricated by electrochemical etching of a 9 mil diameter, poly-crystalline tungsten (W) wire. Although a variety of electrochemical tip preparation methods have been developed over the years [31], our group has perfected a reliable drop-off etch method that is capable of producing tips with radius of curvature of ∼10 nm. The W tips were electrochemically etched in a 3 M and 0.5 M NaOH solution made with ultra-high purity, deionized water. The electrochemical cell consists of a gold ring anode and W wire cathode, as shown in Fig. 3.3. The gold ring is dipped in a 3 M NaOH solution to form a thin meniscus, before the W wire is inserted vertically through the meniscus. A DC bias of 7-10 V is supplied to trigger the

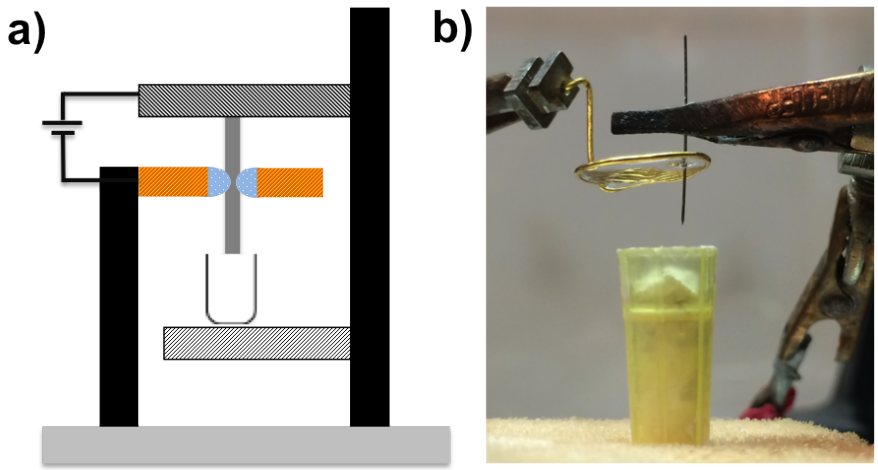

Figure 3.3: (a) Illustration of the electrochemical tip etching system, showing the W wire (cathode), gold ring (anode) and DC power supply. (b) Actual image of tip etching system.

following electrolysis reaction:

$$6\,H_2O + 6\,e^- \longrightarrow 3\,H_2(g) + 6\,OH^-(anode)$$

$$W(s) + 8\,OH^- \longrightarrow {WO_4}^{2-} + 4\,H_2O + 6\,e^-(cathode)$$

$$W(s) + 2\,OH^- + 2\,H_2O \longrightarrow {WO_4}^{2-} + 3\,H_2(g)$$

Once the tip is sufficiently etched/thinned, the 3 M electrolyte solution is replaced with a 1 M solution. This allows for a slower etching rate and prevents excessive bubbling and surface roughening. The lower portion of the W wire eventually drops off once the etching is complete, resulting in a sharp tip. By automatically creating an open circuit during the drop-off, this method prevents overetching of the tip, which would result in a blunt tip. Following the drop-off, the tips were rinsed in DI water and carefully blow-dried with nitrogen. The tips were then loaded onto tip holders, which were subsequently attached to a tip heater, and degassed in UHV by heating for 12-16 hours.

3.3 Sample Preparation

In order to carry out the STM study of the grown 1T-TaS_2, we had to select a suitable substrate and a devise a clean and reliable method to transfer the material of interest onto our substrate. All of the following STM studies were performed on a hydrogen-passivated, highly P-doped silicon substrate. The H-passivated substrate provides an inert, atomically flat and conductive substrate that is suitable for STM experiments.

To prepare the H-passivated silicon samples, we first scribed clean, highly B-doped, Si (100) wafers to an appropriate size that is compatible with our STM sample holders. The samples were then sonicated in acetone and isopropyl alcohol (IPA) and mounted onto the sample holder with tantalum spacers; tantalum spacers, owing to their high conductivity and melting point, protect the sample holder during high temperature processes. Care must be taken to avoid the use of stainless steel tweezers when handling the silicon samples in order to avoid nickel contamination of the surface.

The sample holder was then transferred to the prep chamber, where the sample was resistively heated through the dipstick electrical feedthroughs. During the 12-18 hr degas, the sample is maintained at about 650 °C. At this elevated temperature, adsorbed contaminants desorb from the surface and get pumped out through the vacuum pumps. Following the degas, the surface was passivated to satisfy the dangling bonds on the surface. The sample was first rapidly heated to 1250 °C to remove the surface native oxide, carbide, and any lingering contaminants. This rapid heating process is typically referred to as a flash. As observed in a few instances, during these flashes, or any high temperature for that matter, sudden change in temperature cause the sample to expand and crack. The samples need to mounted with care to achieve even and uniform contact without too much stress on the substrate. After a series of flashes, the hydrogen passivation was done at 377 °C. During the passivation step, the prep chamber is filled with H_2 gas, which is cracked using a W cracking filament to form hydrogen radicals.

The hydrogen dosing was performed for 10 minutes to achieve a 1200 L dose, which is sufficient to fully passivate the surface.

When Si is cleaved along the (100) surface, silicon's ideal tetrahedral structure is interrupted at the silicon surface. Each of the surface atoms have two unsatisfied dangling bonds, creating a high energy surface and attempts to relax by reconstructing to a lower-energy structure. In order to reduce the number of unfulfilled bonds by half, the silicon atoms on the surface bond with each other along the (001) direction, as seen in Fig. 3.4.

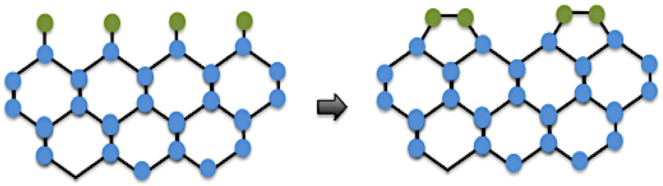

Figure 3.4: Surface atoms (shown in green) have two unsatisfied bond before dimerization. The energy of the system is reduced when the surface atom bonds with their neighbor to give a 2 x 1 reconstruction of the surface.

The resulting dimers give a surface with filled and unfilled rows with a 2 x 1 periodicity. The distance between adjacent dimers in a row is 3.84 Å and the distance between adjacent dimers is 7.68 Å. The remaining dangling bonds are satisfied with the hydrogen atoms during H-passivation. Figure 3.5 shows a 300 Å x 300 Å topographic and current image of the passivated surface. The dimer rows, with measured periodicity of 9.2 Å - 9.8 Å are clearly visible in the scan. Also some debris/contaminants can be seen in a few areas. Figure 3.6 shows a 900 Å x 900 Å scan of a cleaner area of the silicon substrate with almost no debris.

The bright spots in the image correspond to dangling bonds that were left unpassivated during the H-passivation procedure. With a lack of hydrogen atom, it is reasonable to expect a depression at the site of these dangling bond during a topographic scan of the surface. However, the STM scan reveals the dangling bond as a protrusion above the surface, since the silicon dangling bonds have conductive surface states; the tip retracts when crossing these dangling bond sites to maintain a constant current. We also observe that the direction of the dimer

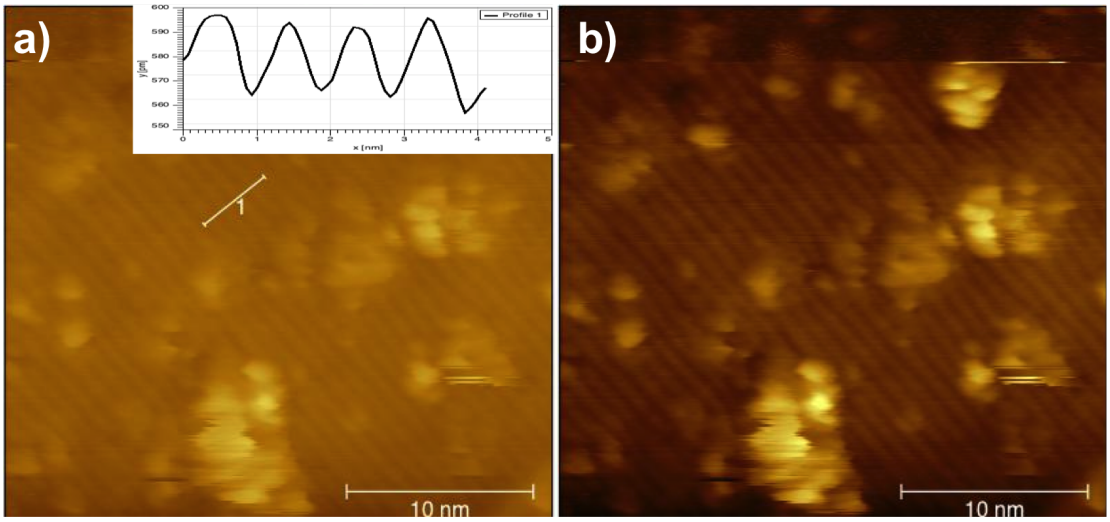

Figure 3.5: (a) Topographic scan of H-passivated silicon. Although some debris is spotted on the surface, we can image silicon dimer rows. Inset shows the height profile along the cut line 1 and the measured dimer row spacing is 9.2 Å - 9.8 Å. (b) Dimer rows are resolved better in the current (I) image of the same scan area. (scanning condition: -2 V, 0.2 nA)

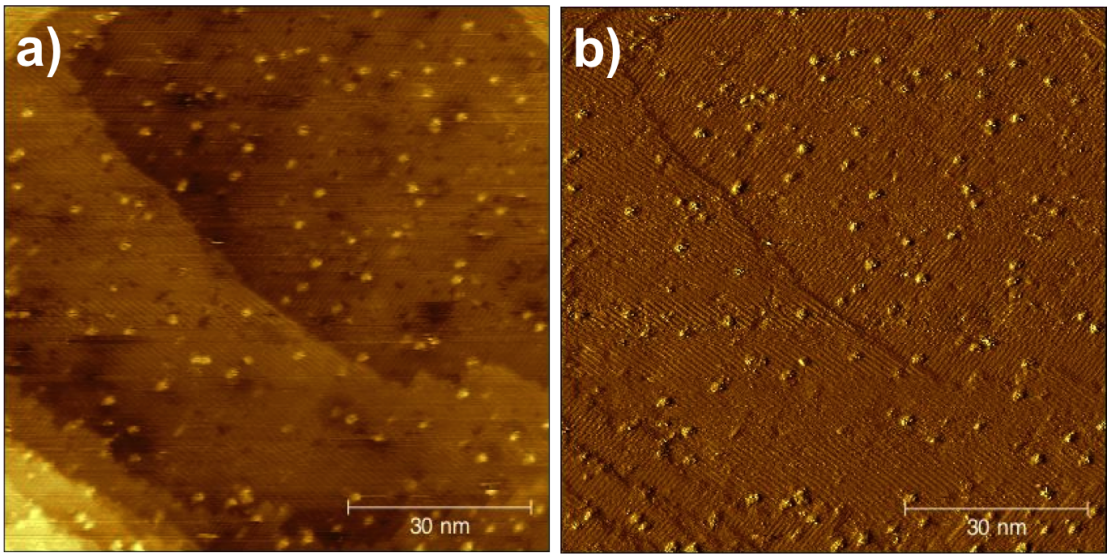

Figure 3.6: (a) Topographic scan of H-passivated silicon. We see clean, large silicon terraces. (b) Current buffer from the same scan. The dangling bonds manifest as bright spots in the these images. (scanning condition: -2 V, 0.2 nA)

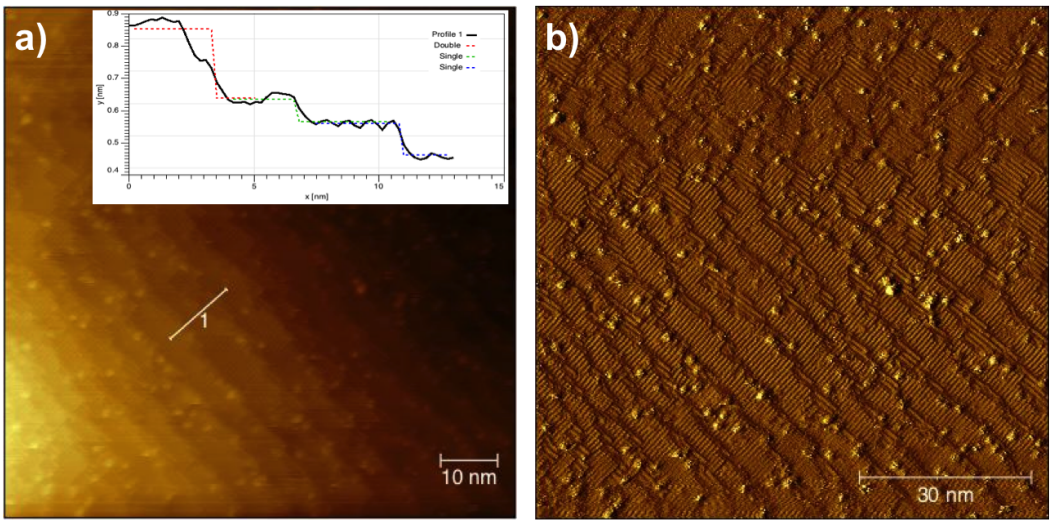

Figure 3.7: (a) Topographic scan of a highly faceted H-passivated silicon. Both single atomic steps (dimer rows rotated by 90°) and bi-atomic steps are observed (parallel dimer rows). Inset shows the height profile at single (0.9 Å) and double (2.1Å) steps. (b) Current buffer from the same scan; unsatisfied dangling bonds manifest as bright spots. (scanning condition: -2 V, 0.2 nA)

rows rotates by 90 degrees when crossing atomic-height steps, since the direction of the dangling bonds rotates through 90 degrees on passing from the higher terrace to the lower terrace. Those steps that are parallel to the upper terrace dimer rows are called "A" steps and those perpendicular are called "B" steps. In certain highly faceted areas, we also observe double steps, where the dimer rows in the two terraces run in parallel to one another, as seen in Fig. 3.7.

3.4 Dry Contact Transfer

In order to perform our STM study of single-layer or few-layer 1T-TaS_2, we need a UHV compatible technique to exfoliate atomically thin layers from the material grown using the bulk growth techniques. A popular technique for obtaining atomically thin layers of 2D material rely on mechanical exfoliation using a scotch tape. As seen in Section 1.2, this method works well for transferring monolayer films on insulating SiO_2, but do not work well for the clean H-passivated silicon substrates prepared for STM study. In a similar pursuit for a UHV-compatible

transfer technique, an *in-situ* dry deposition technique was pioneered by the Lyding group in 2003 [32]. This dry deposition technique was first developed for a clean transfer of single-wall carbon nanotubes (SWCNTs) with minimal perturbation to the UHV-prepared, H-passivated silicon surface. Since the 1T-TaS_2 layers are also separated from one another by a weak van der Waal's force, we can use this same technique to transfer monolayer to few layer 1T-TaS_2 onto our silicon substrate.

The DCT applicators were fabricated by loading a braided, fiberglass sheath, which is then attached to an STM sample holder. The granulated bulk-polycrystalline 1T-TaS_2 was first ground to a fine powder using a mortar and pestle. Subsequently, we loaded the fiberglass sheath by gently rubbing it on the powdered 1T-TaS_2. The fiberglass sheath was then bent to form a loop and attached to the STM sample holder, as shown in Fig. 3.8a. The black 1T-TaS_2 powder is clearly visible on the fiberglass loop. Finally, in order to remove any physisorbed water and other contaminant molecule, the STM sample holder was transferred to the prep chamber for a 12 hour degas. Once the applicator degas was completed, layers of 1T-TaS_2 were transferred by gently contacting the sample with the applicator. We can overcome the weak van der Waal's forces and cleave atomically thin layers of material from the applicator. This step was repeated many times to ensure a high density of 1T-TaS_2 features and enable easier location of these features while performing STM scans. Figure 3.8b shows an illustration of the DCT process.

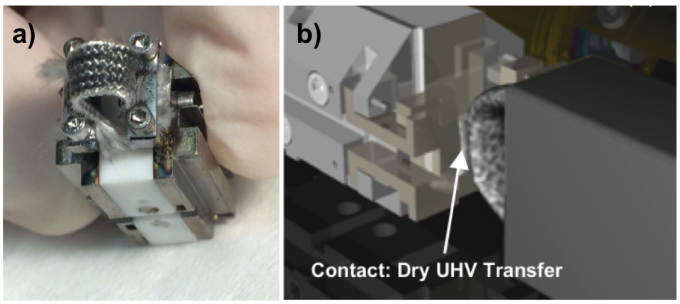

Figure 3.8: a) Image of the DCT applicator, showing the loaded fiberglass sheath attached to an STM sample holder. Black 1T-TaS_2 powder can be seen on the fiberglass sheath. b) A 3D rendering of the DCT method (courtesy of Prof. Joseph Lyding).

3.5 CDW in 1T-TaS_2

Once the poly-crystalline 1T-TaS_2 was transferred by DCT, we searched the silicon surface for deposited flakes of 1T-TaS_2. Although the DCT process is an elegantly simple process to achieve clean, *in-situ* transfer of 2D materials, it does pose a few challenges. Since we do not have strong control on the amount or location of the depositing material, in our search for an ideal flake for this study, we took several scans around different areas of the sample—an ideal flake would be a flat, monolayer or few-layer flake that is at least a few nanometers wide.

Figure 3.9a shows a topographic scan of a large 1T-TaS_2 flake deposited via the DCT method. The flake has a lateral dimension of 105 x 60 nm. The flake appears to be atomically flat with some debris on and around the flake. Also, to the right of the large flake, we see a smaller flake of dimensions 23 x 23 nm. Although the imaging appears streaky away from the flake, the imaging is stable around the region where the flakes were deposited. Figure 3.9 also shows the height profiles at the various cuts. The step heights of 1.09 nm are consistent across all cut lines. Many different exfoliation studies of TaS_2 on SiO_2 have reported monolayer TaS_2 step heights on 1 nm [33, 34]. The flakes observed here have a similar step height and are likely to be monolayers.

Figure 3.10 shows the current buffer from the same scan. Due to the fast scanning condition, the current buffer resolves features better than the height buffer. For all the flakes in the image, we can discern a periodic super-lattice with a threefold symmetry that is significantly larger than the atomic lattice. Figure 3.10 also shows two cut lines that are 60 degrees from one another and their corresponding current profile. The current maxima, which correspond to charge density maxima, have a period of 1.24 nm $\pm$ 0.07 nm. This relates very closely to theoretical prediction. As shown in the inset of Fig. 3.10, the lattice distortion in 1T-TaS_2 gives rise to charge maxima centered on 13-atom Star of David clusters. The theoretical spacing between these clusters is $\sqrt{13}$ a_0 (=1.21 nm), where a_0, the atomic lattice constant, is 3.345 Å. Our experimental result from the STM

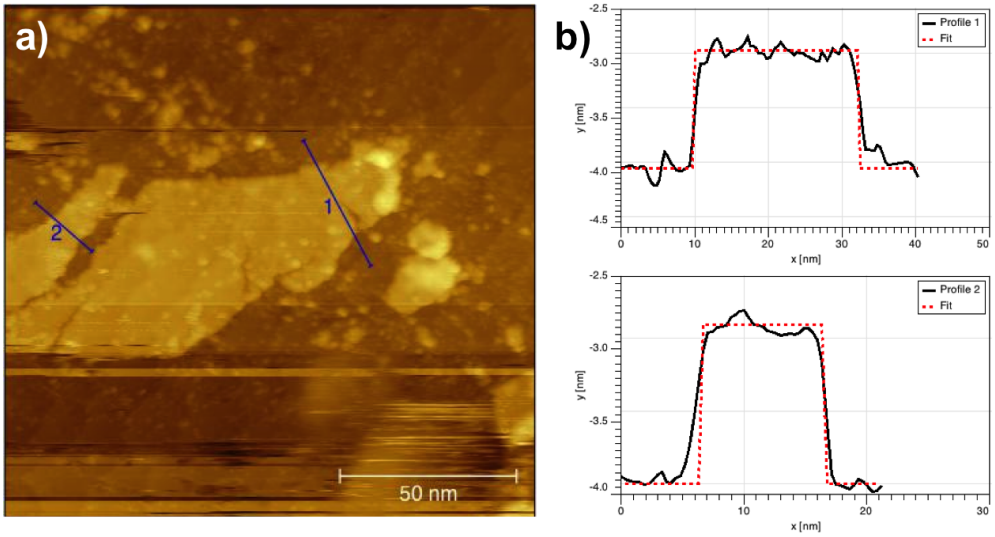

Figure 3.9: (a) 1500x1500Å topographic scan of an area with 1T-TaS_2 flakes, with two cutlines. (b) Height profile across the two cut lines. Step height measures at 1.09 nm and is consistent across different cuts. (scanning condition: -2 V, 0.2 nA)

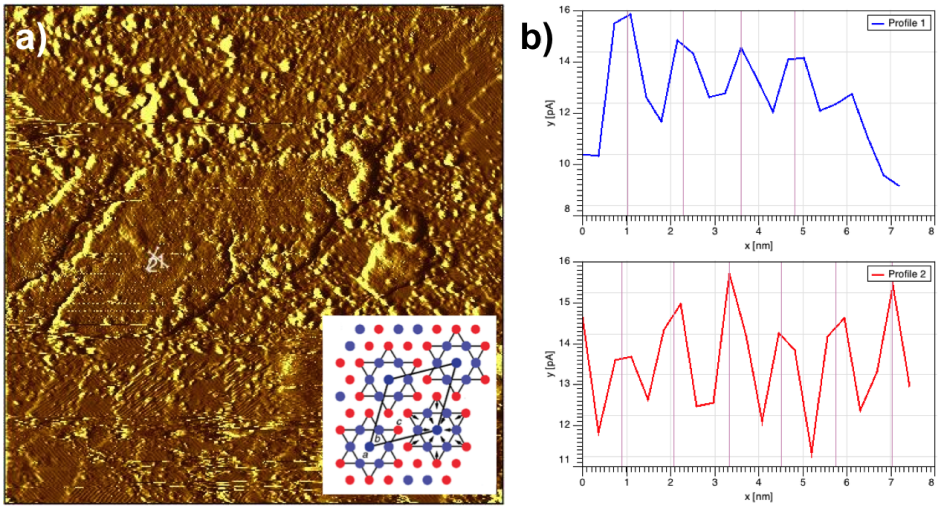

Figure 3.10: (a) Current buffer from the scan shown in Fig. 3.9. Inset shows the Star of David atomic distortion in 1T-TaS_2 [35]. The two cut lines run 60 degrees to one another. (b) Current profile across the two cut lines show consistently periodic peaks (period = 1.24 nm $\pm$ 0.07 nm). Local charge density maxima are separated by $\sqrt{13}$ a_0. (scanning condition: -2 V, 0.2 nA)

study matches very closely with this theoretical value. We have hereby managed to utilize the STM as an effective tool to directly observe the charge density wave phenomenon in real-space; the local charge maxima and minima manifest as current crests (more filled states, higher tunneling current) and troughs (lesser filled states, lower tunneling current).

We further probed the larger flake to try to comprehend the commensurability of charge density wave with respect to the atomic lattice. This required a smaller scan with precise atomic resolution. Figure 3.11 show a zoomed-in current buffer image. Current profiles 1 to 4 show the current variation across the different cut lines. As expected, the periodicity is once again consistent with the theoretical value. However, one should note that while the cut line 1(3) and 2(4) are 60 degrees apart, the two sets of cuts are not perfectly aligned with one another. There is some rotational mismatch and the perfect superlattice structure is broken between the two regions. This is also seen at other locations across the flake. In essence, although we observe periodic CDW superlattice the long range order is disrupted at various areas of the flake. This can be attributed to the pinning of the charge density wave in the presence of impurities and or structural defects. Many studies have been conducted on the strong and weak pinning of charge density waves at impurities and/or defect sites [36–38]. Depending on the relative strength of the pinning energy and the elastic energy needed to deform the CDW, there could be strong or weak pinning of the CDW. The CDW goes through a phase shift at each impurity site (strong pinning) or over a larger length scale (weak pinning), and thereby destroying the perfect long-range order. As we can clearly see from our STM scan, the flake under study has both surface contaminants and structural defects (a large tear is visible on the left side of the big flake), and is far from pristine. The disruption of the long-range order could be attributed to these flaws in the deposited material.

Although the CDW superlattice is clearly resolvable, resolving the atomic lattice proved particularly challenging. Even with ample and generous tip conditioning, it was a struggle to get atomic resolution with the electrochemically etched tips.

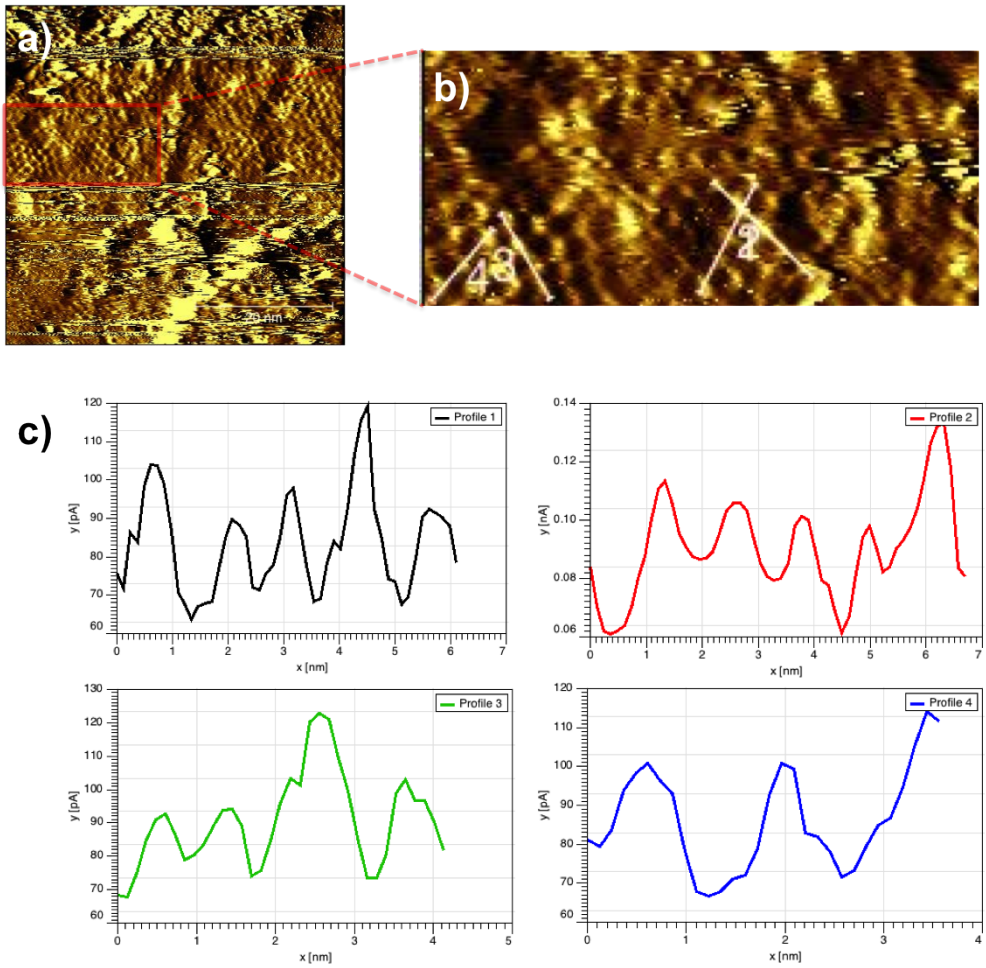

Figure 3.11: (a) Zoomed-in image of the current buffer from the scan shown in Fig. 3.9. (b) The location of the four cut lines are shown. (c) Current profile across the four cut lines show consistently periodic peaks (period = 1.24 nm ± 0.07nm), which matches closely with the theoretical value of $\sqrt{13}$ a_0.

The current profiles in Fig. 3.11 might hint on some partial atomic resolution. Except for current profile 4, we see little kinks adjacent to the current peaks. These kinks could be from a superposition of the underlying atomic lattice with the CDW superlattice. However, we cannot be certain this is the case without a better tip/scan. As an alternative to the in-lab prepared tips, we resorted to commercially available tips from Tiptek. Tiptek, co-founded by Professor Joseph Lyding, is a commercial manufacturer of scanning probe microscopy tips. Tiptek's propriety manufacturing methods allow for an ultra-sharp tip with a radius of curvature of < 4 nm, which could prove very useful in our CDW phase study of

1T-TaS_2. Figure 3.12a shows a post-DCT scan of the H-passivated silicon surface using Tiptek's ultra-sharp tip. Although there seems to be a few tip changes during the span of the scan, the quality of imaging has been vastly improved. Although the features on the surface could be flakes of 1T-TaS_2, these flakes are too small for any meaningful STM study. Figure 3.12b shows 200 Å x 200 Å high-resolution scan from the same area as in Fig. 3.12a. Unlike the scans from the in-lab prepared tips, the periodicity within the dimer rows is now distinctly visible; the height profile across and along the dimer rows clearly illustrate the 2 x 1 reconstruction of the silicon surface.

Also, some spectroscopy measurements were taken on the smaller flakes (diameter < 5 nm), but the spectroscopy did not yield any meaningful measurements

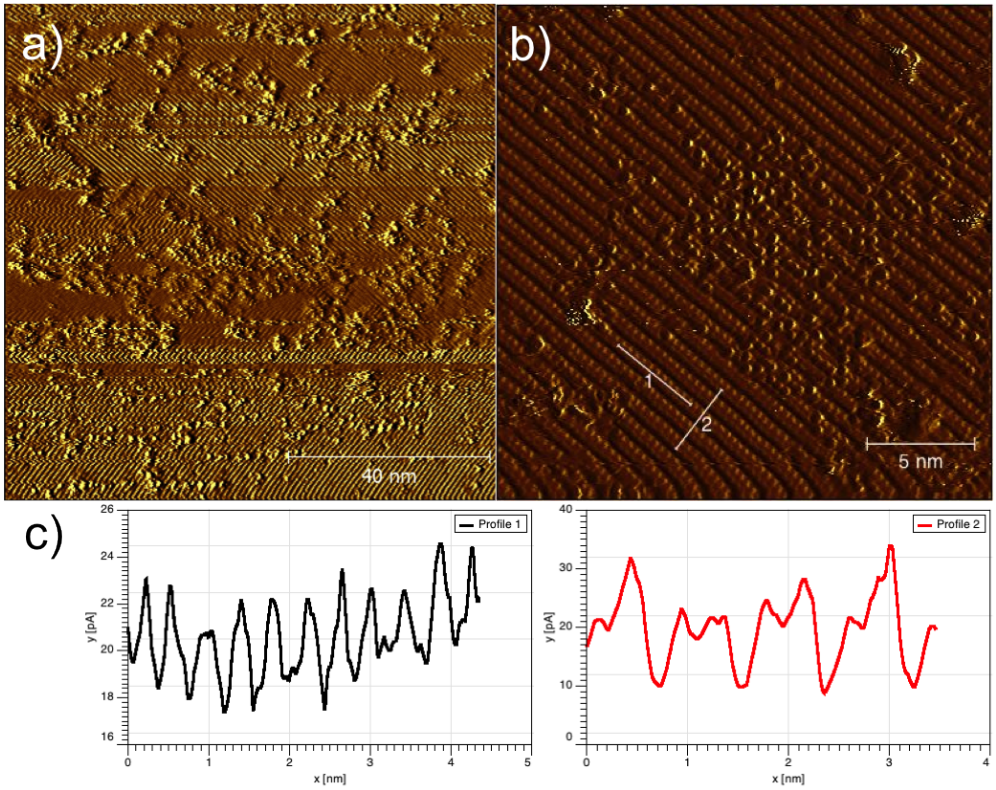

Figure 3.12: (a) Current buffer from a post-DCT scan of the surface. The surface was scanned using a Tiptek tip. Although some tip changes occurred, dimer rows are clearly resolvable. (b) High-resolution 200Å x 200Å image with clearly resolved dimer rows. (c) Step profile along and across the tube indicate 2 x 1 reconstruction of the surface. (scanning condition: -2 V, 0.2 nA)

from the flake—only background silicon IV curve was captured. Defining the precise position for spectroscopy within the scan window proved challenging for these small flakes due to significant thermal drift. At the same time, zooming in on the flake with very small scan windows made the imaging very unstable. The only workaround for this was through the scanning of larger (several 10s of nm), atomically flat flakes. Armed with the exemplary imaging capability of the commercially manufactured tips from Tiptek, we are currently in the pursuit of locating large-area flakes and studying its CDW phase in greater detail (see Chapter 4). With atomic resolution, we can confidently correlate the atomic lattice with the CDW superlattice and further prove the nearly commensurate room-temperature CDW phase of 1T-TaS_2.

CHAPTER 4

SUMMARY AND FUTURE WORK

In this thesis, we have not only utilized the STM for the direct, real-space observation of the room-temperature CDW phenomenon in monolayer 1T-TaS_2, we have also set up the infrastructure required for bulk growth of 1T-TaS_2. Delightfully, these growth techniques are not unique to 1T-TaS_2. This strategy can be extended/modified to grow other materials within the same class of TMDCs, or even other low-dimensional materials such as transition metal trichalcogenide; these simple, yet powerful, bulk growth techniques will pave the path for the synthesis and study of other layered materials. Two bulk growth strategies were developed through the course of this thesis research: direct synthesis of poly-crystalline powder growth and single-crystal growth using CVT. Through several setup modifications, the growth processes were refined to demonstrate repeatable, high-yielding growth of 1T-TaS_2.

The grown poly-crystalline material was subsequently analyzed and characterized by UHV-STM. After preparing sharp tips and atomically flat H-passivated silicon surface, we deposited the polycyrstalline 1T-TaS_2 material on the H-passivated surface using an *in-situ* deposition technique developed by the Lyding lab. STM scans of the material have confirmed monolayer deposition and the existence of the charge density wave superlattice. Although, we clearly see the CDW superlattice with 1.24 nm periodicity, we do not see the larger hexagonal domains, as seen in STM study of bulk TaS_2 crystals (see Section 1.5.2). Any long-range ordering of the CDW superlattice are interrupted by structural defects and/or impurities.

With the use of sharper tips, we now plan on investigating the room-temperature

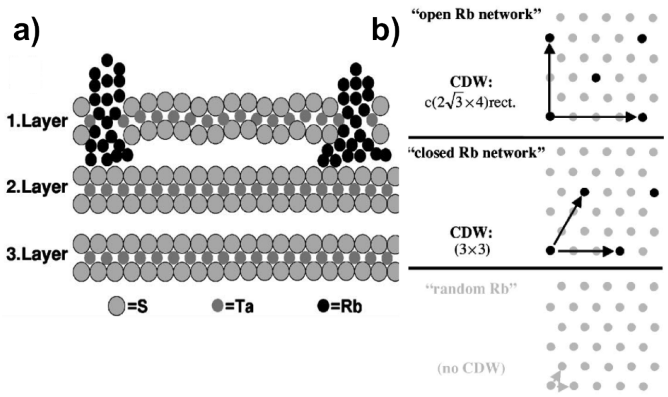

Figure 4.1: (a) Patterning of 1T-TaS_2 nanostructures using growth of Rb nanowires. These nanostructures modified the nearly commensurate room temeparature phase CDW phase as shown in (b) [40].

CDW phase of monolayer 1T-TaS_2 in greater detail. With sharper tips we can get a higher-resolution image that will elucidate the overlap of the atomic lattice and CDW lattice and be crucial in the understanding of the CDW phase. Also we can tap into the process variability of the DCT approach and locate flakes of different thicknesses and record the change in the CDW behavior as a function of layer thickness. As observed by Dr. Kyle Ritter, a previous member of the Lyding group, graphene flakes deposited using the DCT technique have a distribution consisting of 82% monolayers, 11% bilayers, and 7% three-to-five layers thick graphene [39]. Although we have also predominantly found single-layer flakes with step heights of 1-1.1 nm, we do expect some bi-layer and tri-layer deposition.

Having observed and confirmed the CDW phenomenon, we can also now prod further and try to engineer/manipulate the charge density wave using some STM tip-based approach. Many STM tip-based lithography experiments have been demonstrated by the Lyding lab and the STM community. We could use a similar STM lithography strategy to manipulate the surface and CDW behavior. For example, we could selectively break Ta-S bonds and create line defects along the surface; in between two adjacent lines, there could potentially be a quasi-1D structure. By converting the material from a quasi-2D plane to a quasi-1D line, we expect to drastically change the CDW behavior in the material. In 2001, by

growing Rb nanowires on the surface of the layered 1T-TaS_2 and forming a nano-structured surface (Fig. 4.1a), a group managed to modify the room-temperature CDW phase of the material [40]. Depending on the random orientation of the nano-structures formed during the growth, they found various CDW orientations across the surface (Fig. 4.1b). With STM lithography we can repeat this study with more precise control; we can engineer the surface controllably and create nano structures aligned to different crystal facets, which could potentially unveil more CDW phase modification and lead to better fundamental understanding of the CDW behavior in this material.

Through this thesis work, we have laid a solid foundation for further studies of CDW in not only 1T-TaS_2, but other low-dimensional materials. Through several revision of the growth setup, the bulk growth techniques used in this thesis have matured significantly over the course of this research. Furthermore, we have effectively imaged the CDW superstructure on mono-layer 1T-TaS_2. Armed with the poly-crystalline powder growth, single-crystal CVT growth and DCT, we have all the necessary tools in our arsenal to perform novel and exciting research in this field of study.

APPENDIX A

FURNACE MAINTENANCE

This appendix will outline the modifications made to restore the 1000 Series Marshall Tube furnace in order to restore its two-zone functionality. Even though the furnace was sold as a two-zone furnace (two separate windings/zones—left and right zone), the furnace was essentially operating as a single-zone furnace; the controllers were unable to drive any current to the right zone in order to heat up the zone. A "dead" right zone was not a concern in the initial poly-crystalline growth experiments, since there was no need for any controlled temperature gradients; however, for single-crystal growth under a temperature gradient [20], it was imperative to mend this problem and restore the "dead" right zone.

In order to diagnose the problem systematically, different parts of the furnace system were tested individually. During power up, the self-diagnostic function in the controller verifies all the sensor calibration data, controller status flags and user adjustable parameters stored in the non-volatile memory. The self-diagnostics passed without throwing any error flags. Once the controller passed its self-diagnostic test, the controller and furnace connections were then manually verified. After ruling out the controller half of the furnace, we took a closer look at the furnace windings themselves. A possible cause for the lack of current drive could be a highly resistive winding; the windings could have easily burnt out or oxidized after years of persistent operation. It was highly convenient that the furnace was shunt-tap furnace with eight external leads. Even though their primary purpose was to improve temperature uniformity by allowing shunt resistor connections, the shunt taps also provided external connections to the winding, which could be used to probe individual sections of the winding, as shown in Fig.

A.1. The diagram shows a single zone winding and its shunt tap connections.

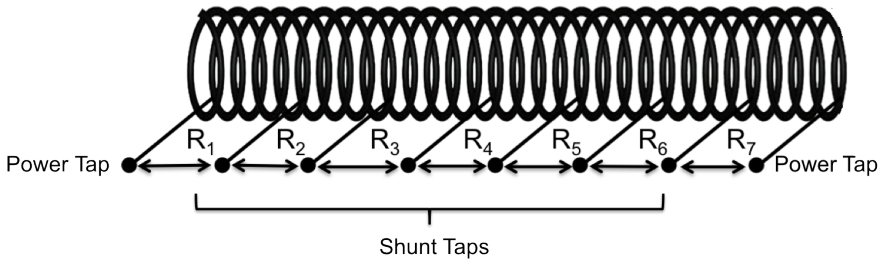

Figure A.1: Tube furnace winding with external power and shunt taps.

Table A.1: Winding Resistance, Ω

	$\mathbf{R_1}$	$\mathbf{R_2}$	$\mathbf{R_3}$	$\mathbf{R_4}$	$\mathbf{R_5}$	$\mathbf{R_6}$	$\mathbf{R_7}$
Left Zone	**1.6**	**1.6**	**1.3**	**1.4**	**1.6**	**1.5**	**1.5**
Right Zone	**1.5**	**1.6**	**1.5**	**3000**	**0.6**	**1.1**	**1.6**

By using a digital multimeter, we can the probe the resistance across seven smaller subsections of the winding. Table A.1 shows the resistance measurements across the different taps for both the left and right zone. The source for the lack of current drive becomes immediately apparent; since the highly resistive portion of the winding increases the total load on the controller, the controller cannot operate outside of its load ratings and supply adequate current to heat the furnace. Having established the root cause for the problem, we searched for quick and effective solution to solve the problem. A slow and expensive solution would involve the overhauling of the faulty furnace winding and replacing it with a new one. Although this might be an effective approach in the long run, this approach would have incurred high cost and large system downtime. Instead, we decided to hack a quick solution that would appreciably reduce the downtime and accelerate the project timeline. We shorted the resistive portion (R_4) of the winding by connecting a wire across the shunt taps. In order to handle the large current draw, an appropriate gauge wire with a maximum current rating of 14 A (Panoma Electronics - B series) was selected. One of the major drawbacks with this solution

was the lack of current through the resistive portion of the winding, which gives rise to a "cold" subzone within zone. Although, the overall temperature non-uniformity in zone increased from 7 °C to 25 °C (for a set-point temperature of 400 °C), by careful placement of the ampule, we can improve the temperature uniformity within the geometry of the ampule. Also, the temperature uniformity improves the longer the furnace soaks at a particular set-point temperature.

The ampules were placed away from the "cold" subzone as shown in Fig. A.2 and a coaxial thermocouple was used to measure the local temperature near the ampule and provide feedback to the controller.

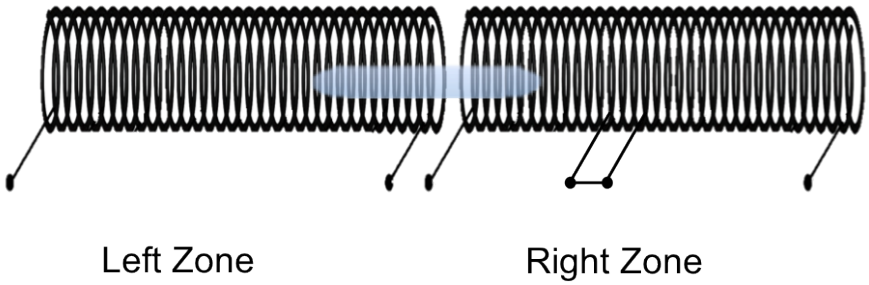

Figure A.2: Illustration of a two-zone furnace with a wire short to bypass the resistive winding. The ampule is placed away from the "cold" subzone and a coaxial thermocouple setup is used to measure local temperature in the right zone.

Further maintenance were also performed throughout the course of this thesis work; faulty Barber Coleman controllers were swapped multiple times and eventually replaced by the newer, more reliable Red Lion Temperature Setpoint Controller (TSC).

REFERENCES

[1] D. Hisamoto, W.-C. Lee, J. Kedzierski, H. Takeuchi, K. Asano, C. Kuo, E. Anderson, T.-J. King, J. Bokor, and C. Hu, "Finfet-a self-aligned double-gate MOSFET scalable to 20 nm," *Electron Devices, IEEE Transactions on*, vol. 47, no. 12, pp. 2320–2325, December 2000.

[2] K. Bolotin, K. Sikes, Z. Jiang, M. Klima, G. Fudenberg, J. Hone, P. Kim, and H. Stormer, "Ultrahigh electron mobility in suspended graphene," *Solid State Communications*, vol. 146, no. 910, pp. 351 – 355, 2008. [Online]. Available: http://www.sciencedirect.com/science/article/pii/S0038109808001178

[3] A. K. Geim and K. S. Novoselov, "The rise of graphene," *Nat Mater*, vol. 6, no. 3, pp. 183–191, March 2007. [Online]. Available: http://dx.doi.org/10.1038/nmat1849

[4] S. J. Chae, F. Gne, K. K. Kim, E. S. Kim, G. H. Han, S. M. Kim, H.-J. Shin, S.-M. Yoon, J.-Y. Choi, M. H. Park, C. W. Yang, D. Pribat, and Y. H. Lee, "Synthesis of large-area graphene layers on poly-nickel substrate by chemical vapor deposition: Wrinkle formation," *Advanced Materials*, vol. 21, no. 22, pp. 2328–2333, 2009. [Online]. Available: http://dx.doi.org/10.1002/adma.200803016

[5] X. Li, C. W. Magnuson, A. Venugopal, R. M. Tromp, J. B. Hannon, E. M. Vogel, L. Colombo, and R. S. Ruoff, "Large-area graphene single crystals grown by low-pressure chemical vapor deposition of methane on copper," *Journal of the American Chemical Society*, vol. 133, no. 9, pp. 2816–2819, 2011, pMID: 21309560. [Online]. Available: http://dx.doi.org/10.1021/ja109793s

[6] X. Li, W. Cai, J. An, S. Kim, J. Nah, D. Yang, R. Piner, A. Velamakanni, I. Jung, E. Tutuc, S. K. Banerjee, L. Colombo, and R. S. Ruoff, "Large-area synthesis of high-quality and uniform graphene films on copper foils," *Science*, vol. 324, no. 5932, pp. 1312–1314, 2009. [Online]. Available: http://www.sciencemag.org/content/324/5932/1312.abstract

[7] W. A. de Heer, C. Berger, X. Wu, P. N. First, E. H. Conrad, X. Li, T. Li, M. Sprinkle, J. Hass, M. L. Sadowski, M. Potemski, and G. Martinez, "Epitaxial graphene," *Solid State Communications*, vol. 143, no. 12, pp. 92 – 100, 2007, exploring graphene recent research advances. [Online]. Available: http://www.sciencedirect.com/science/article/pii/S0038109807002980

[8] H. Huang, D. Wei, J. Sun, S. L. Wong, Y. P. Feng, A. H. C. Neto, and A. T. S. Wee, "Spatially resolved electronic structures of atomically precise armchair graphene nanoribbons," *Sci. Rep.*, vol. 2, December 2012. [Online]. Available: http://dx.doi.org/10.1038/srep00983

[9] J. Cai, P. Ruffieux, R. Jaafar, M. Bieri, T. Braun, S. Blankenburg, M. Muoth, A. P. Seitsonen, M. Saleh, X. Feng, K. Mullen, and R. Fasel, "Atomically precise bottom-up fabrication of graphene nanoribbons," *Nature*, vol. 466, no. 7305, pp. 470–473, July 2010. [Online]. Available: http://dx.doi.org/10.1038/nature09211

[10] Q. H. Wang, K. Kalantar-Zadeh, A. Kis, J. N. Coleman, and M. S. Strano, "Electronics and optoelectronics of two-dimensional transition metal dichalcogenides," *Nat Nano*, vol. 7, no. 11, pp. 699–712, November 2012. [Online]. Available: http://dx.doi.org/10.1038/nnano.2012.193

[11] I. Song, C. Park, and H. C. Choi, "Synthesis and properties of molybdenum disulphide: From bulk to atomic layers," *RSC Adv.*, vol. 5, pp. 7495–7514, 2015. [Online]. Available: http://dx.doi.org/10.1039/C4RA11852A

[12] H. RamakrishnaMatte, A. Gomathi, A. Manna, D. Late, R. Datta, S. Pati, and C. Rao, "MoS2 and WS2 analogues of graphene," *Angewandte Chemie International Edition*, vol. 49, no. 24, pp. 4059–4062, 2010. [Online]. Available: http://dx.doi.org/10.1002/anie.201000009

[13] Radisavljevic B., Radenovic A., Brivio J., Giacometti V. and Kis A., "Single-layer MoS2 transistors," *Nat Nano*, vol. 6, no. 3, pp. 147–150, March 2011. [Online]. Available: http://dx.doi.org/10.1038/nnano.2010.279

[14] Y. Zhan, Z. Liu, S. Najmaei, P. M. Ajayan, and J. Lou, "Large-area vapor-phase growth and characterization of MoS2 atomic layers on a SiO2 substrate," *Small*, vol. 8, no. 7, pp. 966–971, 2012. [Online]. Available: http://dx.doi.org/10.1002/smll.201102654

[15] K.-K. Liu, W. Zhang, Y.-H. Lee, Y.-C. Lin, M.-T. Chang, C.-Y. Su, C.-S. Chang, H. Li, Y. Shi, H. Zhang, C.-S. Lai, and L.-J. Li, "Growth of large-area and highly crystalline MoS2 thin layers on insulating substrates," *Nano Letters*, vol. 12, no. 3, pp. 1538–1544, 2012, pMID: 22369470. [Online]. Available: http://dx.doi.org/10.1021/nl2043612

[16] Q. Ji, Y. Zhang, T. Gao, Y. Zhang, D. Ma, M. Liu, Y. Chen, X. Qiao, P.-H. Tan, M. Kan, J. Feng, Q. Sun, and Z. Liu, "Epitaxial monolayer MoS2 on mica with novel photoluminescence," *Nano Letters*, vol. 13, no. 8, pp. 3870–3877, 2013, pMID: 23899342. [Online]. Available: http://dx.doi.org/10.1021/nl401938t

[17] X. Zhu, Y. Sun, X. Zhu, X. Luo, B. Wang, G. Li, Z. Yang, W. Song, and J. Dai, "Single crystal growth and characterizations of Cu0.03TaS2 superconductors," *Journal of Crystal Growth*, vol. 311, no. 1, pp. 218 – 221, 2008. [Online]. Available: http://www.sciencedirect.com/science/article/pii/S0022024808010841

[18] V. Maksimov, N. Baranov, V. Pleschov, and K. Inoue, "Influence of the mn intercalation on magnetic properties of TiSe2," *Journal of Alloys and Compounds*, vol. 384, no. 12, pp. 33 – 38, 2004. [Online]. Available: http://www.sciencedirect.com/science/article/pii/S0925838804005468

[19] F. J. DiSalvo and J. V. Waszczak, "Magnetic studies of VSe2," *Phys. Rev. B*, vol. 23, pp. 457–461, January 1981. [Online]. Available: http://link.aps.org/doi/10.1103/PhysRevB.23.457

[20] M. Binnewies, R. Glaum, M. Schmidt, and P. Schmidt, "Chemical vapor transport reactions: A historical review," *Zeitschrift fr anorganische und allgemeine Chemie*, vol. 639, no. 2, pp. 219–229, 2013. [Online]. Available: http://dx.doi.org/10.1002/zaac.201300048

[21] S. van Smaalen, "The Peierls transition in low-dimensional electronic crystals," *Acta Crystallographica Section A*, vol. 61, no. 1, pp. 51–61, January 2005. [Online]. Available: http://dx.doi.org/10.1107/S0108767304025437

[22] B. Sipos, A. F. Kusmartseva, A. Akrap, H. Berger, L. Forro, and E. Tutis, "From Mott state to superconductivity in 1T-TaS2," *Nat Mater*, vol. 7, no. 12, pp. 960–965, December 2008. [Online]. Available: http://dx.doi.org/10.1038/nmat2318

[23] X. L. Wu and C. M. Lieber, "Hexagonal domain-like charge density wave phase of TaS2 determined by scanning tunneling microscopy," *Science*, vol. 243, no. 4899, pp. 1703–1705, March 1989.

[24] A. Pisoni, J. Jacimovic, O. S. Barii, A. Walter, B. Nfrdi, P. Bugnon, A. Magrez, H. Berger, Z. Revay, and L. Forr, "The role of transport agents in MoS2 single crystals," *The Journal of Physical Chemistry C*, vol. 119, no. 8, pp. 3918–3922, 2015. [Online]. Available: http://dx.doi.org/10.1021/jp512013n

[25] G. Binnig, H. Rohrer, C. Gerber, and E. Weibel, "Surface studies by scanning tunneling microscopy," *Phys. Rev. Lett.*, vol. 49, pp. 57–61, July 1982. [Online]. Available: http://link.aps.org/doi/10.1103/PhysRevLett.49.57

[26] J. Lyding, "UHV STM nanofabrication: Progress, technology spin-offs, and challenges," *Proceedings of the IEEE*, vol. 85, no. 4, pp. 589–600, April 1997.

[27] L. Haggerty and A. M. Lenhoff, "STM and AFM in biotechnology," *Biotechnology Progress*, vol. 9, no. 1, pp. 1–11, 1993. [Online]. Available: http://dx.doi.org/10.1021/bp00019a001

[28] Y. Levi, O. Millo, N. D. Rizzo, D. E. Prober, and L. R. Motowidlo, "Scanning tunneling microscope studies of the superconductor proximity effect," *Phys. Rev. B*, vol. 58, pp. 15 128–15 134, December 1998. [Online]. Available: http://link.aps.org/doi/10.1103/PhysRevB.58.15128

[29] C. G. Slough, W. W. McNairy, R. V. Coleman, B. Drake, and P. K. Hansma, "Charge-density waves studied with the use of a scanning tunneling microscope," *Phys. Rev. B*, vol. 34, pp. 994–1005, July 1986. [Online]. Available: http://link.aps.org/doi/10.1103/PhysRevB.34.994

[30] T. W. Michael Schmid, "The scanning tunneling microscope," http://www.iap.tuwien.ac.at/www/surface/stm_gallery/stm_schematic, 2011, [Online; accessed April 5, 2015].

[31] A. J. Melmed, "The art and science and other aspects of making sharp tips," *Journal of Vacuum Science & Technology B*, vol. 9, no. 2, pp. 601–608, 1991. [Online]. Available: http://scitation.aip.org/content/avs/journal/jvstb/9/2/10.1116/1.585467

[32] P. M. Albrecht and J. W. Lyding, "Atomically clean integration of carbon nanotubes with silicon," *AIP Conference Proceedings*, vol. 723, no. 1, pp. 173–180, 2004. [Online]. Available: http://scitation.aip.org/content/aip/proceeding/aipcp/10.1063/1.1812067

[33] Q. V. Le, T. P. Nguyen, K. S. Choi, Y.-H. Cho, Y. J. Hong, and S. Y. Kim, "Dual use of tantalum disulfides as hole and electron extraction layers in organic photovoltaic cells," *Phys. Chem. Chem. Phys.*, vol. 16, pp. 25 468–25 472, 2014. [Online]. Available: http://dx.doi.org/10.1039/C4CP04412F

[34] J. Zheng, H. Zhang, S. Dong, Y. Liu, C. Tai Nai, H. Suk Shin, H. Young Jeong, B. Liu, and K. Ping Loh, "High yield exfoliation of two-dimensional chalcogenides using sodium naphthalenide," *Nat Commun*, vol. 5, January 2014. [Online]. Available: http://dx.doi.org/10.1038/ncomms3995

[35] S. Hellmann, M. Beye, C. Sohrt, T. Rohwer, F. Sorgenfrei, H. Redlin, M. Kalläne, M. Marczynski-Bühlow, F. Hennies, M. Bauer, A. Föhlisch, L. Kipp, W. Wurth, and K. Rossnagel, "Ultrafast melting of a charge-density wave in the Mott insulator 1T-TaS_2," *Phys. Rev. Lett.*, vol. 105, p. 187401, October 2010. [Online]. Available: http://link.aps.org/doi/10.1103/PhysRevLett.105.187401

[36] W. Aichmann, "Pinning of charge density waves by strong impurities," *Physica B: Condensed Matter*, vol. 217, no. 12, pp. 1 – 7, 1996. [Online]. Available: http://www.sciencedirect.com/science/article/pii/0921452695005331

[37] H. Dai, J. Liu, and C. Lieber, "Elucidating complex charge density wave structures in low-dimensional materials by scanning tunneling microscopy," in *Advances in the Crystallographic and Microstructural Analysis of Charge Density Wave Modulated Crystals*, ser. Physics and Chemistry of Materials with Low-Dimensional Structures, F. Boswell and J. Bennett, Eds. Springer Netherlands, 1999, vol. 22, pp. 225–257. [Online]. Available: http://dx.doi.org/10.1007/978-94-011-4603-6_7

[38] J. McCarten, M. Maher, T. L. Adelman, and R. E. Thorne, "Size effects and charge-density-wave pinning in $NbSe_3$," *Phys. Rev. Lett.*, vol. 63, pp. 2841–2844, December 1989. [Online]. Available: http://link.aps.org/doi/10.1103/PhysRevLett.63.2841

[39] K. Ritter, "Atomic-scale characterization of nanometer-sized graphene," Ph.D. dissertation, University of Illinois at Urbana-Champaign, 2008.

[40] R. Adelung, J. Brandt, L. Kipp, and M. Skibowski, "Reconfiguration of charge density waves by surface nanostructures on TaS2," *Physical Review B - Condensed Matter and Materials Physics*, vol. 63, no. 16, pp. 1 653 271–1 653 277, 2001, cited by 13. [Online]. Available: http://www.scopus.com/inward/record.url?eid=2-s2.0-0034888924&partnerID=40&md5=6fc490210e79abdcdcad39e502a2a8f4